Cell Biol Toxicol (2025) 41:58
https://doi.org/10.1007/s10565-025-10001-1

RESEARCH

Targeted nanoparticle delivery system for tumor-associated macrophage reprogramming to enhance TNBC therapy

Xiaoshen Dong · Xiaoou Wang · Xinyu Zheng · Haiyang Jiang · Lu Liu · Ningye Ma · Shuo Wang

Received: 7 September 2024 / Accepted: 12 February 2025

Abstract Triple-negative breast cancer (TNBC) poses as a daunting and intricate manifestation of breast cancer, highlighted by few treatment options and a poor outlook. The crucial element in fostering tumor growth and immune resistance is the polarization of tumor-associated macrophages (TAMs) into the M2 state within the tumor microenvironment (TME). To address this, we developed M2 targeting peptide-chitosan-curcumin nanoparticles (M2pep-Cs-Cur NPs), a targeted delivery system utilizing chitosan (Cs) as a carrier, curcumin (Cur) as a therapeutic agent, and targeting peptides for specificity. These NPs effectively inhibited TNBC cell proliferation (~70%) and invasion (~70%), while increasing the responsiveness of tumors to anti-PD-L1 treatment (~50% survival enhancement) in vitro and in vivo. Bioinformatics analysis suggested that Cur modulates TAM polarization by influencing key genes such as COX-2, offering insights into its underlying mechanisms. This study highlights the potential of M2pep-Cs-Cur NPs to reverse M2 polarization in TAMs, providing a promising targeted therapeutic strategy to overcome immunotherapy resistance and improve TNBC outcomes.

Keywords Triple-negative breast cancer · Tumor-associated macrophages · Curcumin · Nanoparticles · COX-2 · Reprogramming · Immunotherapy resistance

Xiaoshen Dong and Xiaoou Wang are contributed equally to this work.

Supplementary Information The online version contains supplementary material available at https://doi.org/10.1007/s10565-025-10001-1.

X. Dong · X. Zheng · H. Jiang · L. Liu · S. Wang (✉)
Department of Surgical Oncology, Breast Surgery, General Surgery, The First Hospital of China Medical University, 155 North Nanjing St, Shenyang 110001, China
e-mail: swang88@cmu.edu.cn

X. Wang
Department of Geriatric Cardiovascular, The First Hospital of China Medical University, 155 North Nanjing St, Shenyang 110001, China

X. Zheng
Lab 1, Cancer Institute, the First Hospital of China Medical University, Shenyang, Liaoning, China

N. Ma (✉)
Department of Obstetrics and Gynecology, Shengjing Hospital of China Medical University, 36 Sanhao Street, Heping District, Shenyang, Liaoning Province, China
e-mail: maningyehead@163.com

Introduction

The classification of triple-negative breast cancer (TNBC) is based on the lack of estrogen receptor (ER), progesterone receptor (PR), and human epidermal growth factor receptor 2 (HER2) expression in breast cancer cases (Derakhshan and Reis-Filho 2022; Hong and Xu 2022; Luo et al. 2022). Due to

Published online: 08 March 2025

the absence of these receptors, TNBC is not responsive to conventional hormone therapy and HER2-targeted therapy, leading to relatively limited treatment options (Derakhshan and Reis-Filho 2022; Yang et al. 2023; Li et al. 2022a, b, c, d). TNBC is associated with poor clinical outcomes, marked by its aggressive nature and a high propensity for recurrence and metastasis, particularly within the first 3–5 years after diagnosis (Yu et al. 2021). According to the Global Cancer Observatory, the year 2024 witnessed the diagnosis of more than 2.3 million instances of breast cancer globally, with TNBC accounting for approximately 10–20% of cases and exhibiting the highest mortality rate among all subtypes. Given the aggressive behavior and poor prognosis of TNBC, novel strategies must be formulated urgently to enhance patient survival rates (Karim et al. 2023; Dass et al. 2021, Popovic et al. 2023).

The involvement of tumor-associated macrophages (TAMs) is notable in the TNBC tumor microenvironment (TME) (Pal et al. 2021; Li et al. 2022a, b, c, d; Wang et al. 2021a, b, c). In TNBC, TAMs predominantly exhibit an M2-polarized phenotype, induced by the unique TME, such as the secretion and accumulation of IL-4, hypoxia, and other factors. These processes drive M2 polarization via transcriptional reprogramming, signal transduction, and metabolic alterations (He et al. 2021). Secretion of cytokines like IL-10 and TGF-β by M2 macrophages (MΦ) is key in mediating anti-inflammatory responses and Th2-associated immune reactions, assisting tumor cells in immune evasion, boosting angiogenesis, and accelerating tumor growth and metastasis. In TNBC, TAMs predominantly exhibit an M2-polarized state, where these MΦ promote tumor cell growth, invasion, and resistance to various treatment modalities (Liu et al. 2024; Huo et al. 2022).

Previous studies found that chitosan (Cs) can regulate inflammatory responses in M2 MΦ (Vasconcelos et al. 2015) and promote M2 MΦ differentiation by modulating CAV1 (Gao et al. 2023). Cs nanoparticles (NPs) have been widely used as drug delivery carriers in MΦ (Jiang et al. 2017), enabling various drugs to modulate M2 polarization for disease treatment (Jiang et al. 2017; Kazimierczak et al. 2021). Moreover, curcumin (Cur), extracted from turmeric (Wang et al. 2023a, b), can reverse M2 polarization in TAMs, inhibit tumor growth and metastasis, and overcome immunoresistance by modulating TAM function (Li et al. 2023; Mukherjee et al. 2020). Previous studies have also shown that Cur affects multiple cellular signaling pathways, influencing TAM behavior and M2 polarization (Gao et al. 2015, Huang et al. 2024). However, these methods have shown limited efficacy in targeting the TME specifically and reliably in vivo.

Academic literature suggests that encouraging the alteration of TAMs from M2 phenotype to M1 phenotype can effectively impede tumor growth and invasion (Fernando et al. 2023). Through the secretion of pro-inflammatory cytokines like IL-12 and TNF-α, M1 MΦ showcases effective antitumor activity, enabling the immune system to identify and remove cancer cells (Ren et al. 2024). The presence of TAMs in the microenvironment of tumors is crucial for enhancing tumor growth and metastasis and inhibit immune responses through activation and polarization toward the M2 phenotype, facilitating immune evasion and drug resistance, especially resistance to immune checkpoint inhibitors like PD-L1 inhibitors. This makes TAMs a potential therapeutic target (Li et al. 2022a, b, c, d; Tkach et al. 2022; Barkal et al. 2019; Wang et al. 2023a, b). Although PD-L1 inhibitors have provided significant survival benefits in TNBC treatment (Cortes et al. 2022; Zhang et al. 2022a, b), the emergence of resistance to PD-L1 blockade over time has become a major obstacle to the sustained efficacy of immunotherapy (Vranic et al. 2021). Thus, exploring and developing strategies to promote TAMs' reprogramming from the M2 to the M1 phenotype has become a focus in TNBC treatment research (Bill et al. 2023; Hao et al. 2022; Wang et al. 2022a, b, c).

Cs, a natural polysaccharide, exhibits excellent biocompatibility, biodegradability, and unique cationic properties, making it highly advantageous for drug delivery. Similar to decorated nanostructured lipid carriers designed for active targeting, Cs can be chemically modified to enhance delivery efficiency and specificity for multiple anti-cancer agents (Mahoutforoush et al. 2021). It interacts with negatively charged biomolecules or cell membranes, facilitating targeted drug delivery, and its surface can be chemically modified, such as grafting targeting peptides or loading hydrophobic drugs, to enhance delivery efficiency and specificity. Among various potential carriers, Cs was chosen for its low toxicity, high

stability, and pH-responsive release in acidic TME (Jiang et al. 2017; Kazimierczak et al. 2021). Studies have shown that Cs can promote M2 MΦ differentiation by regulating CAV1 and participate in modulating inflammatory responses (Vasconcelos et al. 2015, Gao et al. 2023) Furthermore, Cur, a bioactive constituent sourced from turmeric, has demonstrated the capacity to modulate the function of TAMs, reverse M2 polarization, and inhibit tumor growth, metastasis, and immune resistance (Wang et al. 2023a, b; Li et al. 2023; Mukherjee et al. 2020).

Cur also regulates multiple cellular signaling pathways, thereby influencing TAM behavior (Gao et al. 2015, Huang et al. 2024). However, these methods have primarily shown efficacy in vitro or in certain in vivo disease models, while studies on targeting specificity and therapeutic efficacy in the TME remain insufficient. Ensuring the secure and accurate management of TAM behavior in vivo presents a considerable obstacle in research pursuits (Datta and Bangi 2023, Wang et al. 2021a, b, c).

Nanotechnology holds great potential in this regard, as it significantly enhances drug targeting and therapeutic efficacy (Asadollahi et al. 2022; Moradpoor et al. 2021; Husain et al. 2023). Recent studies have demonstrated that methotrexate-functionalized PEGylated nanostructured lipid carriers can achieve targeted delivery of anticancer molecules such as pennyroyal, effectively inhibiting breast cancer cell growth by activating multiple apoptosis pathways. These findings further validate the significant potential of functionalized nanocarriers in targeted drug delivery and therapeutic strategy optimization (Mahoutforoush et al. 2023). NPs, with their unique size and surface properties, can efficiently penetrate biological barriers and deliver drugs directly to the TME (Darvishi et al. 2024; Deng et al. 2022). In this study, we utilized Cs as a nanocarrier combined with targeting peptides to specifically deliver Cur to M2 TAMs. This approach aims to enhance drug delivery efficiency through nanotechnology, achieve precise regulation of TAMs within the TME, and improve the therapeutic outcomes for TNBC.

This research aims to shift TAMs from M2 to M1 polarization by developing M2 targeting peptide-chitosan-curcumin nanoparticles (M2pep-Cs-Cur NPs), thereby inhibiting the growth and invasion of TNBC and enhancing the tumor's sensitivity to immunotherapy. Through detailed bioinformatics analysis and molecular docking experiments, we identified COX-2 as a key gene regulated by Cur in TAM polarization and demonstrated its potential to modulate TAM polarization by affecting the TNF and IL-17 pathways. Furthermore, in combination with anti-PD-L1 therapy, our strategy holds promise for significantly improving TNBC treatment outcomes, offering more effective treatment options for patients. This study not only highlights the application prospects of nanotechnology in cancer therapy but also provides new theoretical foundations and experimental data for future clinical strategies.

Materials and methods

Main materials

Cs (1105508, Sigma-Aldrich), EDTA·2Na (324503, Sigma-Aldrich), acetone (650501, Sigma-Aldrich), glutaraldehyde (8.20603, Sigma-Aldrich), dialysis membrane (MWCO 14 kDa, FDM514m Beyotime), Cur (2 mg, 08511, Sigma-Aldrich), FBS (10099, Gibco), RPMI 1640 medium (11875101, Gibco), DMEM/F-12 medium (21041025, Gibco), PMA (16561–29-8, Sigma-Aldrich), IL-4 (20 ng/mL, 200–04, PeproTech), IL-13 (20 ng/mL, 200–13, PeproTech), 0.5% Triton X-100 (P0096, Beyotime), anti-CD86 rabbit monoclonal antibody (ab239075, 1:100, Abcam, UK), anti-CD163 mouse monoclonal antibody (ab156769, 1:100, Abcam, UK), Alexa Fluor 488/594-conjugated secondary antibodies (ab150077/ab150116, 1:200, Abcam, UK), DAPI (10 μg/mL, D3571, Thermo Fisher, USA), polybrene (TR-1003, Merck), puromycin (540222, Sigma-Aldrich), RIPA lysis buffer (P0013B, Beyotime, China), BCA protein assay kit (P0011, Beyotime, China), HRP-conjugated goat anti-rabbit IgG (ab6721, 1:2000, Abcam), EdU (C0071S, Beyotime), 0.4% crystal violet (C0121, Beyotime), anti-PD-L1 antibody (BE0101, Bio X Cell), isotype control antibody (BE0090, Bio X Cell), anti-Ki67 rabbit antibody (ab16667, 1:200, Abcam), anti-PCNA rabbit antibody (ab92552, 1:500, Abcam), RBC Lysis Solution (158904, Qiagen), anti-CD80-PE (553769, BD Biosciences), anti-CD86-APC (561964, BD Biosciences), anti-CD206-FITC (141703, BioLegend), anti-CD163-APC (155305, BioLegend).

Preparation and characterization of TAMs M2pep-Cs-Cur NPs

Synthesis of M2pep-Cs NPs

The synthesis procedure of Cs NPs entailed the gradual introduction of 3 mL acetone (650501, Sigma-Aldrich) into 2 mL Cs solution (5 mg/mL, 1105508, Sigma-Aldrich) with the incorporation of 1.25 mg EDTA·2Na (324503, Sigma-Aldrich) over a period of 5 min under magnetic stirring at 25 °C and 300 rpm, resulting in a milky-white non-crosslinked NP suspension. Subsequently, 20 µL of glutaraldehyde (25% solution in water, 8.20603, Sigma-Aldrich) was added for crosslinking at pH 6.5 for 4 h. The NPs were then purified by dialysis (MWCO 14 kDa, FDM514m, Beyotime) in distilled water for 48 h. The M2pep peptide (sequence: YEQDPWGVKWWY, 10.27517/d.cnki.gzkju.2021.000532), labeled with Cy5, was synthesized and conjugated to the Cs NPs. To achieve this, 0.5 mg of M2pep (0.27 mmol/L) was included in 1.0 mL of 1.0 mg/mL Cs NPs (< 0.07 mmol/L) and stirred at 200 rpm at room temperature (RT) for 16 h. The NPs, post-centrifugation at a speed of 10,000 rounds per minute for 15 min, were rinsed and rehydrated in deionized water, with the repetitive nature of this rinsing process being threefold. The conjugation efficiency was determined using UV–visible spectroscopy at 280 nm, with an efficiency of approximately 85% (Pang et al. 2019).

Loading of Cur and efficiency calculation

The loading of Cur was carried out using the following steps. 200 µL of a Cur solution (4 mg) (08511, Sigma Aldrich) was added to separate 1 mL suspensions of M2pep-Cs NPs (10 mg, prepared in a Cs solution dissolved in 1% acetic acid and modified to pH 5.0 with 0.1 M NaOH). Sodium triphosphate (TPP, 1 mg/mL, pH 5) was introduced, and the solution was gently mixed in a dimly lit environment at RT for a duration of 12 h. Subsequently, the mixture experienced centrifugal forces at a rate of 10,000 rounds per minute for 10 min to eliminate any Cur that had not been taken up, following which the residue was dispersed in 2 ml of deionized water to generate Cur-loaded NPs, named as M2pep-Cs-Cur NPs. Assessment of the free Cur concentration in the supernatant was executed at 425 nm with the aid of a UV–Vis spectrophotometer (UV-1900, Shimadzu). By applying specific mathematical expressions, the drug loading efficiency (DLE) and drug loading capacity (DLC) were quantified: DLC (%) = (weight of loading)/(weight of NPs + Mass of NPs) × 100%; DLE (%) = (weight of loading)/(Total drug added) × 100%. Measurement of free Cur concentration in the supernatant was carried out via UV–Vis spectroscopy at 425 nm. Under equivalent experimental setups, the calibration chart for Cur was constructed, with interference from degradation products and environmental factors evaluated and accounted for. The trials were triplicated for each data point. Results are expressed as mean ± standard deviation (SD), and statistical significance was assessed through paired or unpaired t-tests for normally distributed data, with $P < 0.05$ indicating statistical significance (Zhou et al. 2014).

Particle size and charge analysis

Through the utilization of dynamic light scattering (DLS) with a Nano-ZS90 apparatus (Malvern, UK) featuring a 633 nm He–Ne laser, the dimensions, polydispersity index (PDI), and zeta potential on the surface of Cs NPs and M2pep-Cs NPs were assessed. The evaluations were completed under constant conditions at 25 degrees Celsius, repeated thrice (Zhou et al. 2014, Khan et al. 2016).

Stability of NPs

Studying the physiological endurance of NPs, they were dissolved in water, saline, PBS, and RPMI 1640, and then cultured for a day. Furthermore, suspension of M2pep-Cs NPs occurred in solutions with different pH levels (4.5, 5.5, 6.5, 7.5, and 8.5). Post a 24-h incubation duration, the dimensions, dispersion, and radiance intensity of NPs were analyzed utilizing DLS. Direct observation indicated the morphology of the NPs using a Hitachi H7650 transmission electron microscope (Hitachi, Japan). Measurements were performed in triplicate (Zhou et al. 2014).

Transmission electron microscopy (TEM) analysis

TEM (Hitachi H7650, Japan) was employed to analyze the morphology of the NPs. Specimens of M2pep-Cs NPs were placed onto copper grids coated with carbon, dried in the air, and subjected to

negative staining with a 1% w/v uranyl acetate solution for a duration of 15 min. Once dried, the samples underwent examination utilizing an accelerating voltage of 120 kV. Captured TEM pictures were scrutinized and interpreted with the Soft Imaging Viewer software for additional investigation. All experiments were conducted in triplicate (Zhou et al. 2014, Khan et al. 2016).

Cur release and cytotoxicity in Vitro

The Cur release curves of M2pep-Cs NPs were assessed in three distinct environments: pH 7.4, pH 6.5, and pH 5.(adjusted from PBS buffer at pH 7.4 using HCl). Put simply, 1 mL of Cur NP(10 μg/mL)-loaded solution with an identified concentration was moved into a dialysis sack (MWCO 3.5 kDa), ensuring the NPs (molecular weight > 14 kDa) remained inside while Cur (molecular weight ~ 0.37 kDa) dispersed and soaked in 5 mL of PBS. Subsequently, all extracts were placed in a 50 ml rotor tube and swirled leisurely in obscurity at 37 degrees Celsius moving at a velocity of 100 rpm. At set time intervals, 5 mL of the buffer solution was extracted and substituted with fresh 5 mL of PBS. The Cur release quantity was detected at 425 nm through UV spectrophotometric analysis. Each measurement was executed thrice. Results are reported as mean ± SD. Analytical computations involved assessments of normality and uniformity of variance, proceeded by unpaired t-tests to compare groups.

Cytotoxicity of Cur

THP-1 cellular entities were introduced into a 96-section container and managed at a temperature of 37 degrees Celsius under 5% CO_2 for a period of 24 h. Following removal of the original medium, 200 μL of new medium with unbound Cur and Cur-loaded NPs (at concentrations of 1.5625 to 50 μg/mL) or M2pep-Cs NPs (at concentrations of 31.25 to 1000 μg/mL, carrying around 5% drug content) was added. Cs NPs without Cur were used as controls. After 48 h of incubation, removal of the medium was conducted, and 200 μL of a fresh medium containing MTT (0.5 mg/mL) was introduced into each well, followed by an incubation in darkness lasting for 4 h. Subsequently, the suspended liquid was gathered, and 150 μL of the solvent DMSO was poured into every well to disintegrate the formazan crystals. After vibrating in the dark for 5 min, each well's light absorption was recorded at 570 nm employing a microplate photometer (E8051, Promega). Computation of cell viability was executed based on the provided formula: Cell viability = (Sample OD570 / Control OD570) × 100% (Wang et al. 2021a, b, c). The investigation was carried out in triplicate, and results from diverse time points were evaluated using two-way analysis of variance (ANOVA).

Cellular uptake

THP-1 cells in 12-well plates were treated with 5 μM Cur, M2pep-Cs NPs (100 μM), and M2pep-Cs-Cur NPs (100 μM, with a drug loading capacity of approximately 5%) for 4 h. After treatment, the cells received three PBS washes and were then set using cold paraformaldehyde for 15 min. Following cell washing, DAPI was applied for a 10-min staining duration. Finally, observations of fluorescence were made utilizing a confocal microscope (Leica, CH) and analyzed using the Image J software. Additionally, cells treated with the drugs were collected, fixed with cold paraformaldehyde, stained with DAPI, and analyzed using flow cytometry (FC500 Beckman, USA) (Zhang et al. 2022a, b). The investigation was duplicated on three occasions.

Construction of the "Curcumin-targets-disease" network

A total of 966 and 63 target genes for Cur were retrieved from the Comparative Toxicogenomics Database (CTD) (https://ctdbase.org/) and the SwissTargetPrediction database (STP) (http://swisstargetprediction.ch/), respectively. By employing the "Venn diagram" software, intersecting genes were distinguished through the Venn diagram visualization. Subsequently, the GeneCards database (https://www.genecards.org/) yielded the leading 100 genetic markers correlated with MΦ. Identifying six common genes between Cur targets and genes associated with MΦ was facilitated by a Venn diagram. Application of the "clusterProfiler" software facilitated the implementation of enrichment analyses for Gene Ontology (GO) and Kyoto Encyclopedia of Genes and Genomes (KEGG). The STRING online platform was utilized to conduct an analysis of protein–protein

interactions (PPI). The assembly of the network "Drug-Targets-Macrophages" was accomplished with the aid of Cytoscape 3.7.2 tool, and network topology parameters were calculated using NetworkAnalyzer for network analysis (Wang et al. 2022a, b, c).

Molecular docking simulation

The Protein Data Bank (https://www.rcsb.org) provided crystal structures for six selected proteins. PubChem data provided the configuration of Cur, which was then transformed into a three-dimensional setup using Chem3D Ultra 14.0 tool, and subsequently underwent energy reduction using the MM2 technique. The utilization of PyMOL software facilitated the preparation of target protein receptors by dehydrating and eliminating organic molecules. The target protein receptor molecules were hydrogenated, charges were calculated, and the conversion of both the compound and target protein receptors to "pdbqt" files was conducted by AutoDockTools 1.5.6. Accurate case focal points and grid parameters were fixed for the docking assessments. Finally, the molecular docking assessment utilized Vina 1.1.2 for calculating the energy values associated with docking (Rosa 2021). Molecular dynamics (MD) simulations of the six protein–ligand complexes were conducted using Amber20 for 100 ns. Root-mean-square deviation (RMSD) trajectories were analyzed, and MMGB/SA modules were used to calculate binding free energies based on stable MD trajectories. Protein systems were parameterized using the AMBER FF14SB force field and solvated in TIP3P water boxes extended by 10 Å. Appropriate counterions were added to neutralize the system.

In vitro cell cultures

Throughout this research, human monocyte MΦ THP-1 (TIB-202, ATCC) were nurtured in RPMI 1640 medium enriched with 10% FBS, while HEK-293 T cells (CRL-3216, ATCC) were maintained in DMEM/F12 medium also supplemented with 10% FBS. Human TNBC cells MDA-MB-231 (CRM-HTB-26, ATCC) and BT-549 (HTB-122, ATCC), as well as mouse TNBC cells 4T1 (CRL-2539, ATCC), were all maintained in a CO_2-regulated incubator (model 51032874, ThermoFisher, USA) with an unchanging 37 °C temperature. Gibco (USA) was the source for the FBS (Catalog number 10099), RPMI 1640 medium (Catalog number 11875101), and DMEM/F-12 medium (Catalog number 21041025).

MΦ activation was initiated by treating THP-1 cells with 320 nM phorbol myristate acetate (PMA) (Sigma-Aldrich, 16561–29-8) for a period of 24 h. The differentiation of M2 MΦ was initiated by treating THP-1 cells with PMA (320 nm) for 6 h, followed by stimulation with IL-4 (20 ng/mL) (PeproTech, 200–04) and IL-13 (20 ng/mL) (PeproTech, 200–13) for a period of 18 h. Subsequently, examination of cell morphology was carried out, and the profiling of cell surface markers was executed (Zhang et al. 2021).

For the co-culture of MΦ and TNBC cells, cancerous cells (1×10^5) were placed in the top compartment of Falcon* Cell Culture Inserts (Corning, Corning, NY), whereas THP-1 monocytes (1×10^6) that had undergone prior treatment were concurrently cultured in the lower compartment. The assessment of invasion was performed by seeding pre-treated THP-1 cells in the lower section of Cell Invasion Inserts (Corning) with RPMI medium containing 10% FBS or a control solution, followed by the analysis of MDA-MB-231 cell invasion (2×10^5) in the upper section after 24 h (Weng et al. 2019).

As per experimental requirements, the cell groups were categorized as follows (NP treatment time and concentration were determined based on cell uptake and toxicity experiments): MΦ group (MΦ), M2 group (M2 MΦ), Control group (M2 cells treated with PBS), M2pep-Cs-Cur NPs group (M2 cells treated with 5 μM M2pep-Cs-Cur NPs for 24 h), oe-NC group (M2 cells as the control group for COX-2 overexpression), oe-COX-2 group (M2 cells with COX-2 overexpression), NPs + oe-NC group (oe-NC cells treated with 5 μM M2pep-Cs-Cur NPs for 24 h), NPs + oe-COX-2 group (COX-2 cells treated with 5 μM M2pep-Cs-Cur NPs for 24 h).

Immunofluorescence experiment

The cells underwent cultivation in glass-bottomed 35 mm cell culture plates (706001, NEST). Immobilization of cellular units was accomplished at RT using 4% paraformaldehyde for 15 min, then subjected to dual PBS washes and permeabilized with 0.5% Triton X-100 (P0096, Beyotime) for a duration of 10 min. The cells then experienced an overnight incubation

at 4 °C with primary antibodies: rabbit anti-CD86 (ab239075, 1:100, Abcam, UK) and mouse anti-CD163 (ab156769, 1:100, Abcam, UK). Upon completion of three PBS washes, the sections were exposed to secondary antibodies tagged with Alexa Fluor 488/594 (ab150077/ab150116, 1:200, Abcam, UK) for one hour. Upon completion of three more PBS washes, the specimens underwent staining with DAPI (10 μg/mL, D3571, Thermo Fisher, USA) for a time span of 10 min at RT. Laser scanning confocal microscopy (Leica, CH) was utilized for the visualization process. ImageJ tool was applied in the analysis of fluorescence (Chen et al. 2022a, b, c). Experimental Groups for M2 MΦ Induction: Control group: PBS-treated M2 MΦ; M2pep-Cs-Cur NPs group: M2 MΦ treated with 5 μM M2pep-Cs-Cur NPs for 24 h; NPs + oe-NC group: oe-NC MΦ treated with 5 μM M2pep-Cs-Cur NPs for 24 h; NPs + oe-COX-2 group: oe-COX-2 MΦ treated with 5 μM M2pep-Cs-Cur NPs for 24 h. The study was replicated in triplicate, and the data derived from the two categories were evaluated through an independent samples t-test.

Cell transfection and cell grouping

Implementing control plasmid oe-NC, target plasmid oe-COX-2 (constructed in pCDH vector), auxiliary plasmid pMD2.G (12259, Addgene), and psPAX2 (12260, Addgene), the lentivirus packaging kit (V48820, Invitrogen, USA) was employed for the transfection of HEK-293 T cells. Post 48 h of transfection completion, the supernatant underwent collection and concentration employing a lentivirus enrichment reagent (631231, Takara), and the concentrated lentivirions were preserved at −80 °C. Upon reaching the logarithmic growth period, THP-1 cells were subjected to trypsin for cell disintegration, and 1×10^5 cells were distributed in each well within a 6-well plate. After incubating the cells for 24 h, and with cell density reaching around 75%, an appropriate dose of lentiviral vectors (initial experiments displayed diverse MOIs for cellular transduction, ultimately validating MOI = 10 at a concentration of roughly 5×10^6 TU/mL) along with 5 μg/mL of polybrene (Merck, TR-1003) were supplemented to the growth medium for transfection. Cell choosing occurred 2 days post lentiviral transduction, with puromycin (540222, Sigma-Aldrich) at a concentration of 10 μg/mL, and the cells with stable transfection were maintained for at least one week (Zhou et al. 2020). Plasmid construction was performed by Shanghai Hanheng Biotechnology Co., Ltd.

RT-qPCR

Trizol reagent (Cat. No. 16096020, Thermo Fisher Scientific, USA) was utilized for the extraction of total RNA from tissues and cells. Utilizing the NanoDrop One/OneC microvolume nucleic acid and protein analyzer by Thermo Scientific, the RNA concentration and quality were inspected, achieving an A260/A280 ratio of 2.0 and a concentration exceeding 5 μg/μL. By employing the first-strand cDNA synthesis kit (D7168L, Beyotime, Shanghai), the RNA was transcribed in reverse and converted into cDNA. Utilizing the RT-qPCR kit (Q511-02, Vazyme Biotech, Nanjing, China), the RT-qPCR investigations were executed according to the manufacturer's instructions. 20 μL of the reaction mixture comprised 2 μL of cDNA template, 0.2 μL of both forward and reverse primers, and 10 μL of RT-qPCR Mix, mixed with RNase-free water. Implementing the Bio-Rad CFX96 real-time PCR system, the PCR amplification process took place under the prescribed settings: initial denaturation at 95 ℃ for 30 s, followed by 40 cycles of denaturation at 95 ℃ for 10 s, annealing at 60 ℃ for 30 s, extension at 72 ℃ for 30 s, and a melting curve analysis from 65 ℃ to 95 ℃. Shengong Biotech (Shanghai, China) furnished and formulated the primer sequences, which can be found in Table S1. The $2^{-\Delta\Delta Ct}$ method was employed to analyze the relative expression of the target gene in the experimental group as opposed to the control group, wherein GAPDH mRNA acted as the reference gene. The formula used was $\Delta\Delta Ct = \Delta Ct_{\text{test}} - \Delta Ct_{\text{control}}$, where $\Delta Ct = Ct_{\text{target}} - Ct_{\text{reference}}$ (Zhang et al. 2019). Experimental Groups: Control group: PBS-treated M2 MΦ; M2pep-Cs-Cur NPs group: M2 MΦ treated with 5 μM M2pep-Cs-Cur NPs for 24 h; oe-NC group: M2 MΦ with COX-2 overexpression control plasmid; oe-COX-2 group: M2 MΦ with COX-2 overexpression plasmid; NPs + oe-NC group: oe-NC MΦ treated with 5 μM M2pep-Cs-Cur NPs for 24 h; NPs + oe-COX-2 group: oe-COX-2 MΦ treated with 5 μM M2pep-Cs-Cur NPs for 24 h. Repetition occurred thrice during the experiment iterations. Two groups were subjected to an independent samples t-test, and multiple groups underwent a one-way ANOVA.

Western blot

Lysis of the total proteins derived from tissues and cells was conducted in RIPA lysis buffer (P0013B, Beyotime, Shanghai) supplemented with 1% PMSF. Quantification of total protein content in every individual sample was conducted through the employment of a BCA assay kit (P0011, Beyotime, Shanghai). With the aim of facilitating electrophoresis separation, SDS gels ranging from 8 to 12% were meticulously prepared to align with the desired sizes of the target protein bands, and loading of protein samples into each lane was uniformly executed with the aid of a microloader pipette. Transferring the proteins from the gel to a PVDF membrane (1,620,177, BIO-RAD, USA) was followed by blocking them with 5% skim milk for one hour at RT. An overnight incubation at 4 °C was conducted following the addition of primary antibodies (Refer to Table S2). Following this, the membrane underwent three washes using 1×TBST at RT, lasting for 5 min per wash. Post the initial incubation process, the membrane was exposed to an HRP-conjugated goat anti-rabbit IgG secondary antibody (ab6721, 1:2000). This exposure lasted for 1 h at RT and the antibodies utilized were obtained from respected suppliers such as Abcam and Cell Signaling Technology. Following three rounds of membrane washing in 1×TBST buffer for 5 min each at RT, ECL substrate (1705062, Bio-Rad, USA) was introduced, enabling the visualization of protein bands via an Image Quant LAS 4000C gel imaging system (GE Healthcare, USA). The internal referencing of GAPDH facilitated the measurement of total protein levels within cells. Grayscale value analysis was utilized with Image J software to determine the relative expression levels of proteins, where the relationship between the target band's grayscale value and the internal reference band's grayscale value indicated the protein expression levels (Wu et al. 2022). Experimental Groups; Control group: PBS-treated M2 MΦ; M2pep-Cs-Cur NPs group: M2 MΦ treated with 5 μM M2pep-Cs-Cur NPs for 24 h; oe-NC group: M2 MΦ with COX-2 overexpression control plasmid; oe-COX-2 group: M2 MΦ with COX-2 overexpression plasmid; NPs + oe-NC group: oe-NC MΦ treated with 5 μM M2pep-Cs-Cur NPs for 24 h; NPs + oe-COX-2 group: oe-COX-2 MΦ treated with 5 μM M2pep-Cs-Cur NPs for 24 h. The repetition was done threefold to validate the results. An independent t-test was executed comparing two groups, with a one-way ANOVA conducted to analyze multiple groups.

Cell growth evaluation utilizing CCK-8 assay

Post cell dissociation and rehydration, the cells were portioned into each well of a 96-well plate at a density of 1×10^3 cells, where they underwent overnight culturing. Cell viability was examined at 0 h, 24 h, 48 h, and 72 h post-culturing based on the instructions provided by the manufacturer of the CCK-8 kit (C0041, Beyotime, Shanghai, China) using the CCK-8 method. The CCK-8 detection solution (10 μL) was introduced cyclically at specified time intervals, undergoing a 1-h incubation in a CO_2 incubator, and then the quantification of optical density at 450 nm was performed with the assistance of a microplate reader (E8051, Promega) (Zhang et al. 2023a, b, c, d). Experimental Groups for Induced M2 MΦ: Control group: PBS-treated M2 MΦ; M2pep-Cs-Cur NPs group: M2 MΦ treated with 5 μM M2pep-Cs-Cur NPs for 24 h; NPs + oe-NC group: oe-NC MΦ treated with 5 μM M2pep-Cs-Cur NPs for 24 h; NPs + oe-COX-2 group: oe-COX-2 MΦ treated with 5 μM M2pep-Cs-Cur NPs for 24 h. Each experiment was conducted in triplicate for statistical reliability. Examination of data involved a two-way ANOVA at disparate time instances.

Detection of cell proliferation rate using EdU labeling

Allocation of three replicates per group was done for cell seeding in 24-well plates. The culture medium received an addition of EdU (C0071S, Beyotime) at a concentration of 10 μmol/L, following which the cells were placed in a CO_2 incubator for 2 h. Upon removal of the culture medium, the cells were immobilized by exposure to a PBS solution containing 4% paraformaldehyde for 15 min at normal RT, followed by permeabilization with 0.5% Triton-100 (HFH10, Invitrogen™, USA) in PBS for 20 min also at RT. Post this step, each well received 100 μL of EdU staining solution and was stored in a light-free environment at regular RT for 30 min. A 5-min incubation period was allotted for the application of DAPI stain (Shanghai Biyun Tian Biotechnology Co., Ltd, Catalog C1002) to specifically target and label the cellular nuclei. Following mounting, a fluorescence

microscope (FV-1000/ES, Olympus, Japan) was utilized to observe 6–10 random fields of view, and the quantity of cells showing positivity in each field was documented. Here is how the EdU labeling rate was computed: EdU labeling rate (%) = (number of positive cells) / (number of positive cells + number of negative cells) × 100% (Shi et al. 2022). Experimental Groups for Induced M2 MΦ: Control group: PBS-treated M2 MΦ; M2pep-Cs-Cur NPs group: M2 MΦ treated with 5 μM M2pep-Cs-Cur NPs for 24 h; NPs + oe-NC group: oe-NC MΦ treated with 5 μM M2pep-Cs-Cur NPs for 24 h; NPs + oe-COX-2 group: oe-COX-2 MΦ treated with 5 μM M2pep-Cs-Cur NPs for 24 h. The trial was reiterated thrice to ensure consistency. The independent t-test method was applied to compare two sets, whereas for multiple sets, a one-way ANOVA analysis was utilized.

Clonogenic assay

In the clonogenic test, the cells designated for examination were dissociated to form individual cell suspensions, with 1000 cells inoculated into every 6 cm petri dish. Scheduled alterations of the complete growth medium were made in each culture dish every three days to ensure optimal growth conditions. The cells were subjected to PBS washing, 4% paraformaldehyde fixation, and a 15-min staining process with 0.4% crystal violet (C0121, Beyotime) post a 10-day incubation period. Manual counting was employed for colonies comprising more than 10 cells, and the average count was obtained from replicate wells for statistical analysis (Zhao et al. 2020). Experimental Groups: Control group: PBS-treated M2 MΦ; M2pep-Cs-Cur NPs group: M2 MΦ treated with 5 μM M2pep-Cs-Cur NPs for 24 h; NPs + oe-NC group: oe-NC MΦ treated with 5 μM M2pep-Cs-Cur NPs for 24 h; NPs + oe-COX-2 group: oe-COX-2 MΦ treated with 5 μM M2pep-Cs-Cur NPs for 24 h. Every trial was duplicated three times. Two groups were subjected to an independent t-test, and in the case of multiple groups, an ANOVA test was utilized.

Transwell invasion assay

The evaluation of in vitro cell invasion was accomplished through the utilization of Transwell chambers (3422, 8 μm pore size, Corning, USA) within a 24-well plate in the performance of the Transwell invasion assay. A culture medium enriched with FBS was introduced into the lower segment of the Transwell unit, which featured a polycarbonate membrane with an 8 μm pore size pre-coated with Matrigel, amounting to 600 mL. Subsequent to incubation at 37 °C for 1 h, the system reached equilibrium. Cells, post enzymatic breakdown, were restored in DMEM medium lacking FBS, and were introduced into the upper compartment with a concentration of 2×10^4 cells/mL, thereafter they were subjected to incubation at 37 °C alongside 5% CO_2 for a duration of 24 h. Upon completion of the experiment within the Transwell chambers, removal of these chambers was carried out, followed by a double rinse with PBS, and later fixed using 5% glutaraldehyde at a temperature of 4 °C. Subsequent to this process, a 0.1% crystal violet staining persisted for 5 min duration, accompanied by the double washing with PBS, and the removal of surface cells was executed by the application of a cotton ball. To facilitate observation, the chambers were inverted and viewed under a fluorescence microscope (Nikon TE2000, China). 5 random fields were photographed, and the mean number of cells that infiltrated the chamber was subsequently computed (Li et al. 2022a, b, c, d). Experimental Groups: Control group: PBS-treated M2 MΦ; M2pep-Cs-Cur NPs group: M2 MΦ treated with 5 μM M2pep-Cs-Cur NPs for 24 h; NPs + oe-NC group: oe-NC MΦ treated with 5 μM M2pep-Cs-Cur NPs for 24 h; NPs + oe-COX-2 group: oe-COX-2 MΦ treated with 5 μM M2pep-Cs-Cur NPs for 24 h. Three repetitions were performed for every individual experiment. The utilization of an independent samples t-test allowed for the comparison of two separate groups, while a one-way ANOVA was utilized to analyze data from multiple groups.

Wound healing assay

Cells from each group in good growth condition were prepared into single-cell suspensions using the previously described method. A six-well plate received a 2 mL cell suspension (4×10^5 cells/mL) after the cell counting process. Cultivation in a CO_2 incubator at 37 °C continued until the cells reached a growth density of 90%−100%. The cell monolayer was subjected to a perpendicular mark using a 200 μL pipette tip, resembling a "scratch". A serum-free medium was poured into the plate after it underwent two

PBS washes to eliminate the suspended cells. After a subsequent 24-h incubation, images were captured, and the scratch distance was measured using Image J software. The calculation method for the relative migration speed is as stated below: relative migration rate = (migration distance of experimental group cells/migration distance of control group cells) × 100% (Jiang 2011). Experimental Groups: Control group: PBS-treated M2 MΦ; M2pep-Cs-Cur NPs group: M2 MΦ treated with 5 μM M2pep-Cs-Cur NPs for 24 h; NPs + oe-NC group: oe-NC MΦ treated with 5 μM M2pep-Cs-Cur NPs for 24 h; NPs + oe-COX-2 group: oe-COX-2 MΦ treated with 5 μM M2pep-Cs-Cur NPs for 24 h. The experiment was iterated threefold to validate the findings thoroughly. Two groups were assessed with an independent t-test, whereas multiple groups were analyzed using one-way ANOVA.

Establishment of the TNBC xenograft mouse model

Procured from Beijing Vital River Laboratory Animal Technology Co., Ltd., China, twenty-four female C57BL/6 J mice, aged 4–5 weeks, were accommodated in a controlled environment at 26–28 °C with a humidity level of 50–65%. Strict adherence to ethical standards was maintained in all animal experiments, as approved by the Institutional Animal Ethics Committee.

During the orthotopic transplantation process, a mixture was prepared containing 4T1 cells, 50% FBS/PBS, and Matrigel (1:1, v/v), to be introduced into the mammary fat pads of female nude mice aged 6 weeks, with each fat pad receiving 2×10^5 cells for the establishment of the 4T1 model. When the tumor reached a size of 10 mm, the animals were randomized into treatment groups. Based on previous studies (Larasati et al. 2018) and in vitro experimental results, dosages of M2pep-Cs-Cur NPs at 10 mg/kg were delivered via tail vein injection every two days, with the control group being treated with an equal volume of PBS. The intraperitoneal injection regimen received by both the Anti-PD-L1 (Bio X Cell, #BE0101) at 12.5 mg/kg and the control group with their specific isotype antibody (Bio X cell, #BE0090) was set at once every 3 days. After the final treatment, mouse serum samples were gathered, and the levels of CK, LDH, ALT, AST, CREA, and urea were gauged employing a fully automated biochemical analyzer (BK-400, Shandong Beike Biotechnology Co., Ltd.). Mice were euthanized by CO_2 inhalation 4 weeks after orthotopic injection, and tissue samples from mammary tumors and essential organs (heart, liver, spleen, lungs, kidneys) were obtained. Preservation methods included fixation in formalin with paraffin embedding or rapid freezing in liquid nitrogen and storage at −80 °C (Lee et al. 2022; Pérez-Núñez et al. 2022).

According to the experimental requirements, the animal grouping is as follows: Control group (PBS-treated TNBC mice), M2pep-Cs-Cur NPs treatment group (TNBC mice treated with M2pep-Cs-Cur NPs), M2pep-Cs-Cur NPs and anti-PD-L1 combination treatment group (TNBC mice treated with M2pep-Cs-Cur NPs and anti-PD-L1), with 6 mice in each group. For RNA-seq analysis: Control group and M2pep-Cs-Cur NPs treatment group, with 3 mice in each group.

Immunohistochemistry

Paraffin embedding was performed for the fixation of tumor tissues in formalin, followed by sectioning. Staining of the sections was conducted through the application of hematoxylin and eosin (H&E), involving a 2-min incubation in hematoxylin and a subsequent 1-min exposure to eosin. Subsequent to dehydration using 70%, 80%, 90%, and 95% ethanol, the sections were treated with xylene twice, with each treatment lasting for 5 min. They were then encapsulated in neutral resin for examination under a BX63 light microscope from Olympus, Japan. The immunohistochemical staining was performed following standard procedures: rabbit anti-Ki67 (ab16667, 1:200, Abcam) and rabbit anti-PCNA (ab92552, 1:500, Abcam) served as the primary antibodies. These antibodies were incubated overnight, followed by a 30-min incubation with goat anti-rabbit IgG (ab6721, 1:1000, Abcam) the succeeding day. The 37 °C incubated sections were treated with SABC (Strept Avidin–Biotin Complex, Vector Labs, USA) for 30 min, then subjected to staining with DAB chromogen solution (P0203, Beyotime Biotechnology, Shanghai) for 6 min before a quick 30-s hematoxylin counterstain. The specimens underwent a dehydration procedure involving a sequence of immersions in solutions of 70%, 80%, 90%, and 95% ethanol, followed by two rounds of exposure to xylene lasting 5 min each. They were subsequently encased in neutral resin for observation using a light microscope

(BX63, Olympus, Japan). Measurement of the staining findings was accomplished via the use of Image J software to gauge both the average gray scale value (intensity of staining) and the quantity of cells exhibiting positive outcomes. Statistical examination was conducted to differentiate variances among distinct sets, and the graphical representation of findings facilitated the assessment of dye impacts on cellular or tissue slices (Zhang et al. 2023a, b, c, d). Employed an independent samples t-test to compare two groups, and conducted one-way ANOVA for analyses involving multiple groups.

Flow cytometry

Tumors obtained were subjected to the following analyses using flow cytometry. Following the manufacturer's instructions, the tumors underwent mincing and enzymatic digestion with the assistance of the MAcs Miltenyi Mouse Tumor Dissociation Kit (130–096–730, Miltenyi Biotec). The separated tumor cells were washed with RPMI Medium 1640, and utilizing the RBC Lysis solution (158904, Qiagen) enabled the lysis of red blood cells. Enumeration and suspension of cells were conducted in PBS solution supplemented with 0.5% BSA and 2 mM EDTA. M1-like and M2-like MΦ were labeled with Anti-CD80-PE (16-10A1, 553769, BD Biosciences), Anti-CD86-APC (GL1, 561964, BD Biosciences), Anti-CD206-FITC (C068C2, 141703, Biolegend), and Anti-CD163-APC (S15049I, 155305, Biolegend) individually (Mehta et al. 2020; Zhang et al. 2021). Two groups were subjected to an independent t-test comparison, and multiple groups underwent a one-way ANOVA analysis for statistical assessment.

Transcriptome sample sequencing and data quality control

In this study, we conducted magnetic bead-based selection of CD11b + cells (Beijing Nuowei Biotechnology, 130–049–601) to isolate MΦ from tumor tissues of Control mice ($n = 3$) and Treat mice (Treat group), proceeded with extracting total RNA by utilizing Trizol reagent (Thermo, 16096020, USA). Subsequently, utilized the Qubit®2.0 Fluorometer® (Life Technologies, Q33216, USA) in conjunction with the Qubit® RNA analysis kit (Shanghai Boji Biotechnology Co., Ltd., HKR2106-01, Shanghai, China), Nanophotometer (IMPLEN, USA), and the Bioanalyzer 2100 system equipped with the RNA Nano 6000 analysis kit (Agilent, 5067–1511, USA) to evaluate the RNA samples' concentration, purity, and integrity. Criteria for RNA evaluation included concentration ($C \geq 20$ ng/μL), purity ($OD260/280 > 2.0$), and integrity ($RIN \geq 7.0$; $28S/18S$ ratio ≥ 1.0).

The starting material for RNA sample preparation encompassed 3 μg of total RNA per sample. In accordance with the recommendations supplied by the manufacturer, the NEBNext® UltraTM RNA Library Preparation Kit designed for Illumina® sequencing (NEB, E7435L, Beijing, China) was applied to craft cDNA libraries. Subsequent quality assessments of these libraries were conducted using the Agilent Bioanalyzer 2100 system. As prescribed by the producer, the indexed samples underwent clustering on the cBot cluster assembly instrument employing the TruSeq PE Cluster Kit v3 cBot HS (Illumina) (PE-401–3001, Illumina, USA). After the generation of clusters, the library preparation step was executed and sequencing was conducted utilizing the Illumina HiSeq 550 platform, producing paired-end reads of 125 bp/150 bp.

Assessment of the quality of paired-end sequencing reads was executed by employing FastQC software version 0.11.8 on the raw sequencing dataset. Adaptors from Illumina sequencing and poly(A) tail sequences were successfully removed from the raw data through preprocessing with Cutadapt software version 1.18. Reads that had a N content of more than 5% were filtered out using a perl script. Subsequently, extracting reads surpassing a base quality score of 20 and constituting 70% of the total bases was achieved using the FASTX Toolkit software version 0.0.13. The paired-end sequences were appropriately fixed with the assistance of the BBMap software. Subsequently, the refined superior read segments were mapped to the mouse reference genetic material through the application of hisat2 software version 0.7.12 (Guo et al. 2023b; Xu et al. 2022).

Transcriptome sequencing analysis

Differential analysis of gene expression comparing Control and Treat samples was performed by utilizing the software tool "Limma" in R, applying criteria of $|log2Fc| > 1$ and $P < 0.001$. The "heatmap" package from R was employed to create visual representations of the differentially expressed genes (DEGs), and the

"ggplot2" package was utilized for generating volcano charts. Creation of Venn diagrams was facilitated by the "vennDiagram" software package. Employing the R package "clusterProfiler," enrichment analyses were performed, shedding light on the pathways of both GO and KEGG for enhanced comprehension (Chen et al. 2022a, b, c).

Statistical analysis

The statistical examination of the bioinformatics outcomes was conducted utilizing R version 4.2.1, while analysis of other data was performed using SPSS version 26.0 (IBM, USA). SD was combined with mean to represent the continuous data. The first step involved conducting tests to evaluate the presence of normality and variance homogeneity. In cases where the data satisfied the criteria of conforming to a normal distribution and having equal variances across groups, t-tests (unpaired for independent samples or paired for related samples) were utilized to compare between groups, while ANOVA or repeated measures ANOVA was employed for comparing multiple groups. A P value below 0.05 was the criterion for determining statistical significance.

Results

Preparation and characterization of TAMs M2pep-Cs-Cur NPs

Despite Cur demonstrating these potentials, research specific to TAMs in TNBC remains relatively scarce. Furthermore, the clinical application of Cur is hindered by its low solubility and limited bioavailability (Hafez Ghoran et al. 2022). In this context, we utilized Cs as a carrier known for its excellent biocompatibility and ability to enhance drug stability through chemical modification (Aghbashlo et al. 2023) to prepare M2pep-Cs-Cur NPs aimed at improving delivery efficiency and therapeutic efficacy. This nanotechnology significantly enhances the delivery performance of Cur, improves the targeting of TAMs M2 cells, and enhances its anti-tumor activity. Figure 1A illustrates the process of preparing M2pep-Cs-Cur NPs.

Initially, the TAMs M2-targeting peptide M2pep was conjugated to the surface of Cs NPs via amide reaction to produce M2pep-Cs NPs. Subsequently, morphology and size attributes of M2pep-Cs NPs were determined by TEM and DLS examinations. The TEM images revealed that both the synthesized Cs NPs and M2pep-Cs NPs exhibited uniform spherical shape and excellent dispersion (Fig. 1B). According to the DLS results, the average hydrodynamic diameter of M2pep-Cs NPs (176 ± 12.6 nm) slightly increased compared to Cs NPs (164 ± 5.12 nm) due to the conjugation of the targeting peptide on the material surface, indicating successful modification of M2pep on Cs NPs. Furthermore, the zeta potential of M2pep-Cs NPs increased to $+75.40 \pm 3.60$ mV compared to Cs NPs ($+66 \pm 5.4$ mV), as shown in Fig. 1C (Table S3). This enhancement indicates an improved stability of the M2pep-Cs NPs system.

To confirm the binding between M2pep and Cs NPs, we employed UV/Visible absorption spectroscopy and fluorescence emission spectroscopy to detect Cy5-labeled M2pep. The UV/Visible absorption spectra analysis of NPs revealed similar Cy5 absorption peaks around 420–480 nm for M2pep-Cs-Cy5 and M2pep-Cy5. Additionally, M2pep-Cs-Cy5 exhibited characteristic emission peaks at 530–550 nm, similar to M2pep-Cy5, providing evidence of successful coupling of M2pep (Fig. 1D).

Subsequently, we synthesized M2pep-Cs-Cur NPs. DLS results showed that the mean particle diameters of M2pep-Cs NPs and M2pep-Cs-Cur NPs were 176 ± 12.6 nm and 182 ± 15.3 nm, respectively, with zeta potentials of $+78 \pm 3.6$ mV and $+70 \pm 5.5$ mV, respectively (Fig. 1E). These results indicate that Cur loading increased the particle size of the NPs without markedly affecting the stability of the system. TEM analysis revealed that both M2pep-Cs NPs and M2pep-Cs-Cur NPs exhibited distinct spherical particles with a dense structure (Fig. 1F), and Cur loading did not alter the structure of M2pep-Cs NPs.

These results demonstrate the successful preparation of TAMs M2pep-Cs-Cur NPs with encapsulation and loading efficiencies of approximately 84% and 5.6%, respectively.

Stability, in vitro release, cellular uptake, and toxicity of M2pep-Cs-Cur NPs

After the successful preparation of M2pep-Cs-Cur NPs, we further investigated the stability of M2pep-Cs-Cur NPs in buffer solutions at varying pH levels using DLS. It was revealed by the results that even

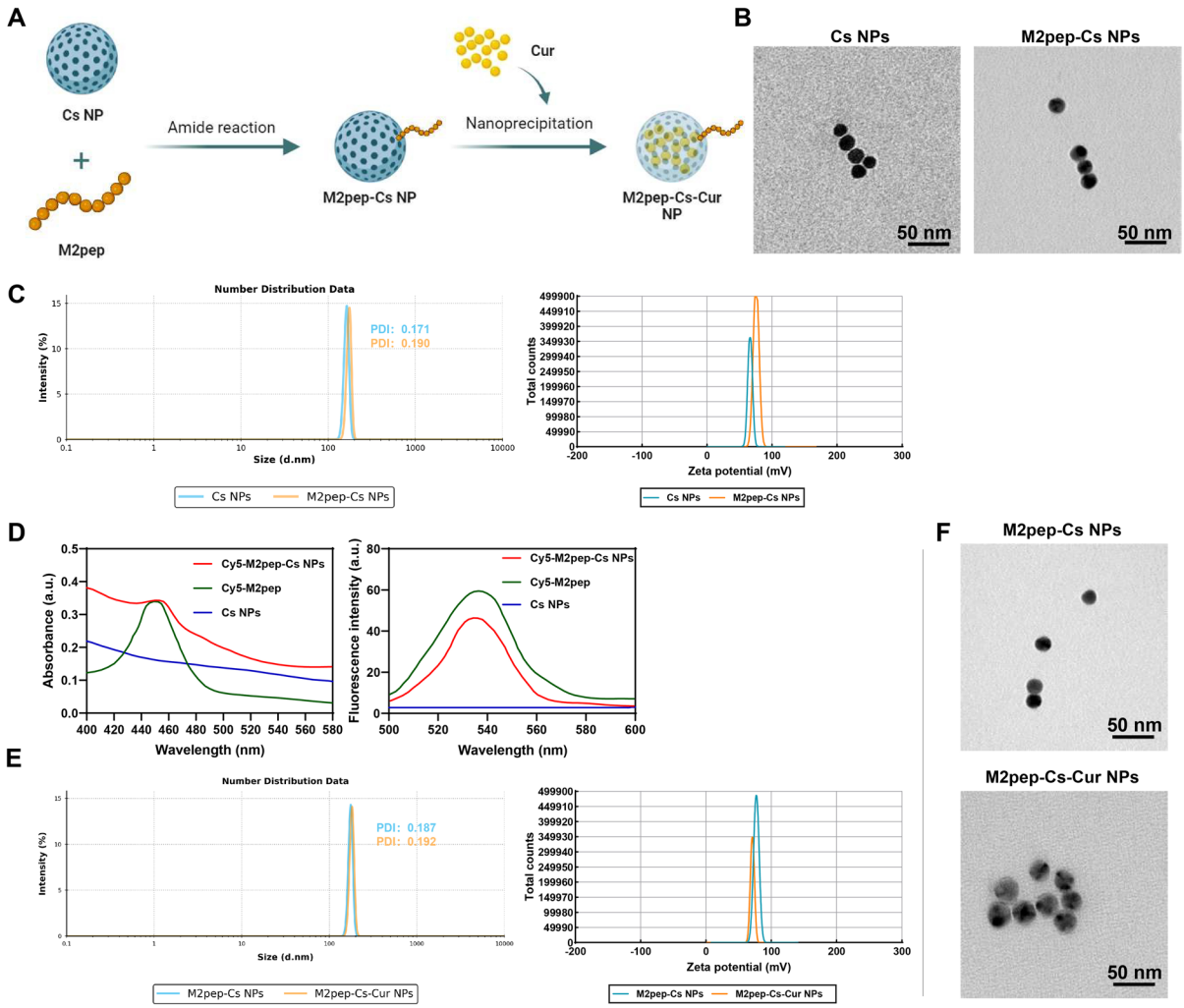

Fig. 1 Preparation and characterization of TAMs M2pep-Cs-Cur NPs. Note: **A** Simple preparation process of M2pep-Cs-Cur NPs; **B** TEM images of Cs NPs and M2pep-Cs NPs (scale = 50 nm); **C** Average hydrodynamic diameter and zeta potential of Cs NPs and M2pep-Cs NPs; **D** UV/Vis absorption spectra and fluorescence emission spectra of Cs NPs and M2pep-Cs NPs; **E** Average hydrodynamic diameter and zeta potential of M2pep-Cs NPs and M2pep-Cs-Cur NPs; **F** TEM images of M2pep-Cs NPs and M2pep-Cs-Cur NPs (scale = 50 nm)

under mildly acidic conditions (pH 5.5 and 6.5), M2pep-Cs-Cur NPs exhibited only slight changes in size and count rates (pH 5.5: 185 ± 2 kcps; pH 6.5: 184 ± 1 kcps) (Fig. 2A). Additionally, the NPs showed minimal size changes and good stability under different physiological circumstances (water, PBS, saline, and RPMI 1640), with count rates consistently near 180 kcps (Fig. 2B). These findings suggest that M2pep-Cs-Cur NPs possess kinetic stability, rendering them suitable as drug carriers.

To investigate the in vitro release rate of Cur from M2pep-Cs-Cur NPs, as well as to explore the controlled release pattern and pH dependence of Cur release from M2pep-Cs-Cur NPs particles, we measured the release curves of Cur in various situations (pH 7.4, pH 6.5, and pH 5.0) (Fig. 2C). The results indicated that at pH 7.4, 6.5, and 5.0, the percentage of Cur released from M2pep-Cs-Cur NPs within the first 2 h was 20%, 30%, and 40% of the total drug, respectively, with an increase in release rate with

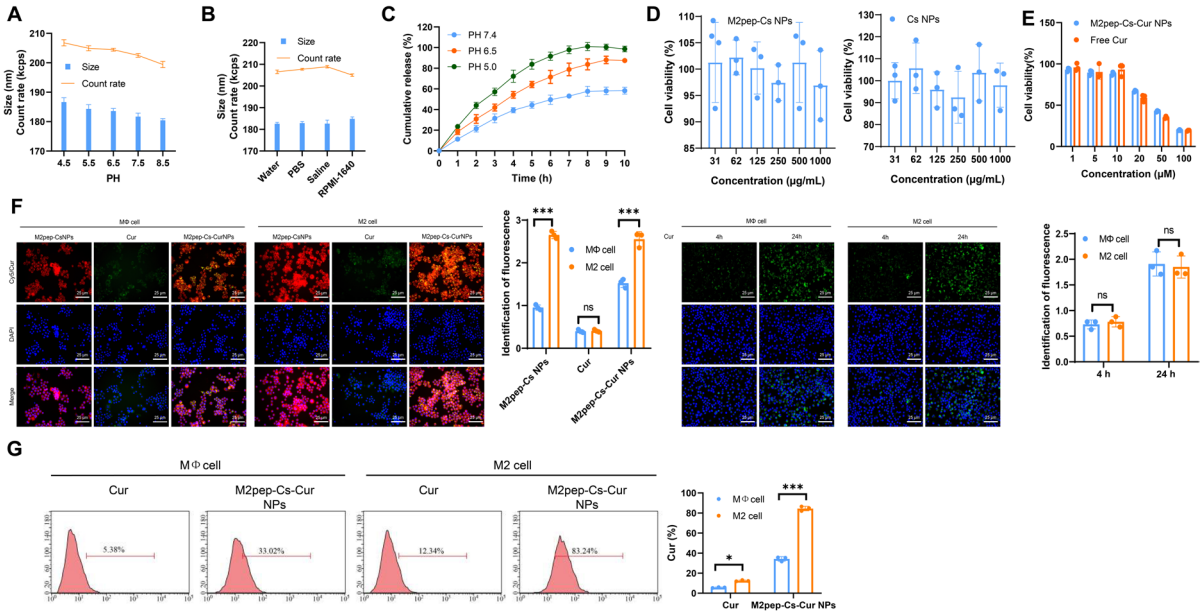

Fig. 2 Stability, in vitro release, cellular uptake, and toxicity of M2pep-Cs-Cur NPs. Note: **A** Stability evaluation of M2pep-Cs-Cur NPs at different pH values; **B** Stability assessment of M2pep-Cs-Cur NPs in various solutions; **C** In vitro release profile of Cur from M2pep-Cs-Cur NPs at different pH values; **D** Cytotoxicity of M2pep-Cs NPs or Cs NPs in THP-1 cells; **E** Dose-dependent cellular toxicity assessment of free Cur and M2pep-Cs-Cur NPs in THP-1 cells; **F** Immunofluorescence detection of cellular uptake of M2pep-Cs NPs, Cur, and M2pep-Cs-Cur NPs *in* M2 MΦ (scale = 25 μm); **G** Flow cytometry analysis of cellular uptake of M2pep-Cs NPs, Cur, and M2pep-Cs-Cur NPs *in* M2 MΦ; $^{ns}P > 0.05$, $^{*}P < 0.05$, $^{***}P < 0.001$; All cell experiments were performed in triplicate

prolonged stirring time. The influence of pH on the release of Cur from M2pep-Cs-Cur NPs is indicated by this finding, implying potentially higher release efficiency in the acidic TME (Chen et al. 2022a, b, c).

Cell toxicity of the M2pep-Cs NPs carrier was evaluated using the MTT assay. The results revealed. That M2pep-Cs NPs and Cs NPs showed no significant cytotoxicity, with cell viability consistently above 90%, indicating good biocompatibility of M2pep-Cs NPs (Fig. 2D). Contrarily, the toxic effects in a dose-dependent manner were examined for free Cur and M2pep-Cs-Cur NPs. Cur showed no effect on cell viability at concentrations below 10 μM. However, the cytotoxicity of the drug increased with higher concentrations, reducing cell viability to below 50% at 50 μM and to approximately 20% at 100 μM (IC50 = 37.05 μM, Fig. 2E). Based on these results, 5 μM was selected for subsequent experiments.

To further investigate the uptake of M2pep-Cs-Cur NPs by MΦ, we induced THP-1 differentiation into MΦ using PMA, succeeded by incubation with IL-4 and IL-13 to obtain M2-polarized MΦ (M2) (validated by detection of the M2 marker protein CD163 to confirm successful polarization (Figure S1)). The uptake of Cur's natural fluorescence and Cy5-tagged M2pep in NPs was monitored using immunofluorescence and flow cytometry methods. The fluorescence exhibited by M2pep-Cs-Cur NPs surpassed that of Cur alone within the M2pep-Cs-Cur NPs cohort, showing a nearly two-fold increase in brightness when tested in M2 MΦ relative to MΦ cells. Nonetheless, the Cy5 fluorescence intensity remained almost identical for both M2pep-Cs NPs and M2pep-Cs-Cur NPs (Fig. 2F). These findings indicated that M2pep facilitated the specific uptake of NPs by M2 MΦ, while the uptake of free Cur by MΦ lacked specificity. Moreover, the majority of Cur and M2pep-Cs-Cur NPs showed colocalization without altering the Cy5 fluorescence. This indicates successful encapsulation of Cur by M2pep-Cs NPs, enhancing the uptake of Cur by M2 cells. Subsequent flow cytometry analysis confirmed this conclusion. Consistent with the immunofluorescence results, the uptake levels

of M2pep-Cs-Cur NPs (~32.8% or ~82.9%) were higher than those of Cur alone (~5.6% or ~12.0%), with the uptake by M2 cells being higher than that by MΦ cells (Fig. 2G).

The results demonstrated that the successfully synthesized M2pep-Cs-Cur NPs exhibited good stability, uniform release in vitro, and efficient uptake by M2 MΦ.

TNBC cell invasion and growth inhibition by M2pep-Cs-Cur NPs through TAM reprogramming

To determine the impact of M2pep-Cs-Cur NPs on M2 cell polarization, we conducted an immunofluorescence analysis of M2 cell polarization-related proteins. The outcomes illustrate a substantial decline in CD163 fluorescence in the M2pep-Cs-Cur NPs-treated group relative to the control group, while the fluorescence of CD86, a protein associated with M1 cells, was enhanced (Fig. 3A). The RT-qPCR outcomes concurred with the immunofluorescence findings, illustrating a decrease in the levels of CD163 and IL-10, common markers for M2 cells, and an elevation in the levels of CD80, CD86, and IL-1β associated with M1 cells (Fig. 3B). These findings indicate that treatment with M2pep-Cs-Cur NPs effectively promotes M2 cell reprogramming.

In order to further investigate whether the reprogramming of M2 cells induced by M2pep-Cs-Cur NPs leads to functional changes in TNBC cells, we co-cultured M2 cells treated with M2pep-Cs-Cur NPs with human TNBC cell lines MDA-MB-231 and BT-549 (designated as NPs-MDA-MB-231 and NPs-BT-549 respectively) (Fig. 3C). The outcomes demonstrated a significant inhibition in the proliferation, migration, and invasion of MDA-MB-231 and BT-549 cells co-cultured with M2 cells treated with M2pep-Cs-Cur NPs (Fig. 3D-G).

These findings indicate that M2pep-Cs-Cur NPs effectively reprogram M2 MΦ, shifting their expression profile from tumor-promoting to anti-tumor. The growth, migration, and invasion of TNBC cells were significantly impeded when exposed to the reprogrammed M2 MΦ in a co-culture scenario, underscoring the potential clinical application of M2pep-Cs-Cur NPs in anti-tumor therapy.

Bioinformatics analysis reveals key genes regulated by Cur in TAMs

To further elucidate the molecular mechanisms underlying Cur's impact on TAM reprogramming, we retrieved 966 and 63 target genes of Cur from the CTD (https://ctdbase.org/) and STP database (http://swisstargetprediction.ch/), respectively. The distribution of target genes in the STP database is illustrated in Figure S2A. By performing a Venn analysis on the predicted target genes from both databases, we identified 49 target genes (designated as "Targets"), as illustrated in Fig. 4A-B. Enrichment analyses based on GO and KEGG pathways revealed that the Targets are primarily enriched in categories related to response to peptide, response to oxidative stress, and cellular response to chemical stress, among others (Figure S2B). The protein interaction network of the Targets is depicted in Figure S2C.

To identify genes associated with MΦ, the GeneCards database (https://www.genecards.org/) provided a list of 100 significant genes correlated with "macrophage". The comparison between MΦ genes and Targets through a Venn diagram revealed 6 target genes that are intricately connected to MΦ: JAK2 (Janus kinase 2, encoding JAK2 protein), STAT3 (signal transducer and activator of transcription 3, encoding STAT3 protein), TNF (tumor necrosis factor, encoding TNFα protein), MMP9 (matrix metallopeptidase 9, encoding MMP9 protein), CSF1R (colony-stimulating factor 1 receptor, encoding CSF1R protein), and PTGS2 (prostaglandin-endoperoxide synthase 2, encoding COX-2 protein) (Fig. 4C-D). Enrichment analysis of these 6 target genes using GO revealed a significant concentration in processes related to inflammation, such as positive regulation of cytokine production, myeloid cell differentiation, and neuroinflammatory response (Fig. 4E). Additionally, KEGG analysis showed a notable enrichment of these genes across various inflammatory signaling pathways, including the JAK-STAT signaling pathway, TNF signaling pathway, Th17 cell differentiation, and IL-17 signaling pathway (Fig. 4F). The enrichment genes corresponding to these pathways are detailed in Table S4. Moreover, protein interaction analysis demonstrated complex interplays among the 6 proteins, indicating their involvement in regulating MΦ polarization (Fig. 4G).

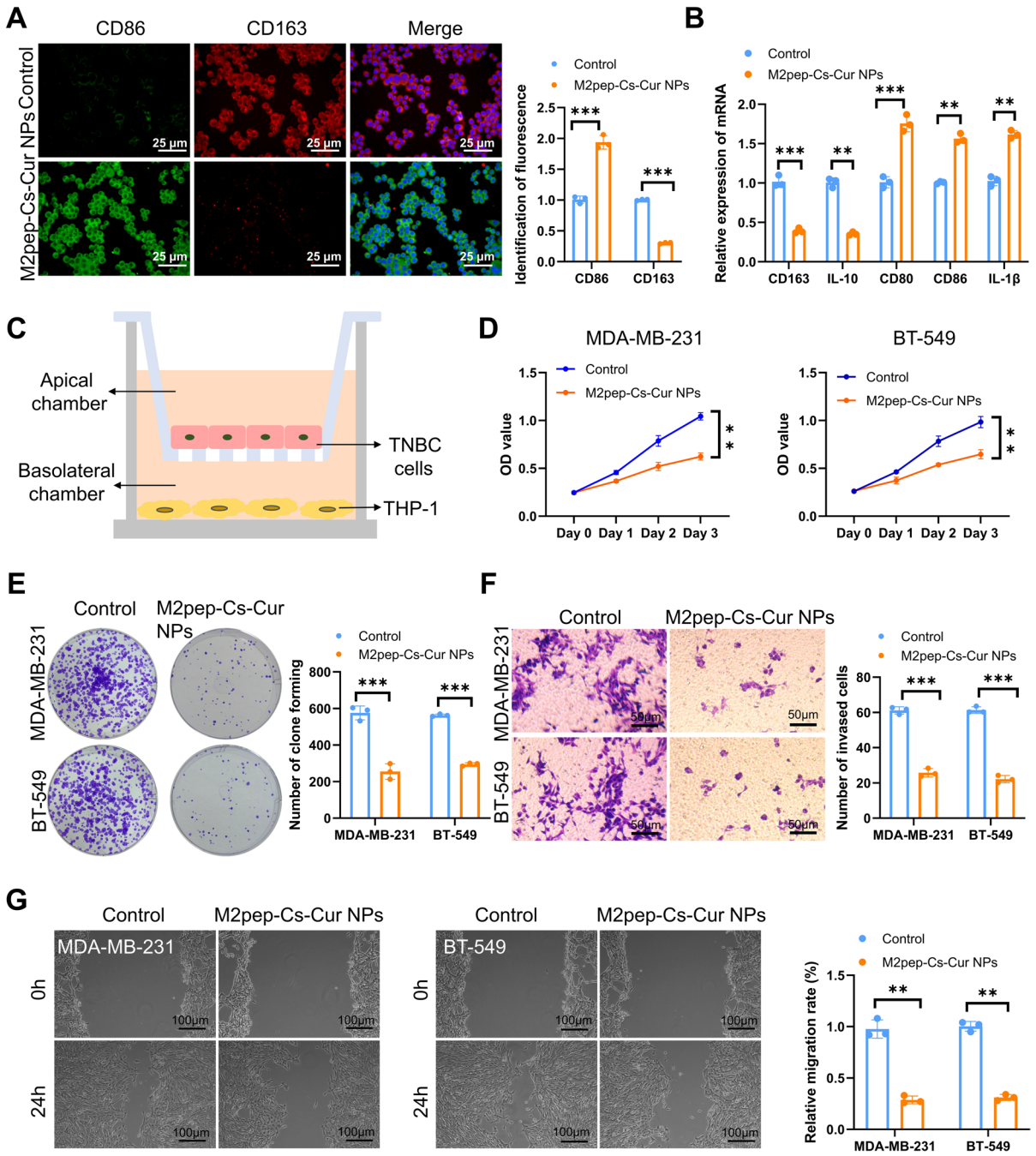

Fig. 3 Impact of M2pep-Cs-Cur NPs on TAMs reprogramming and growth invasion of TNBC cells. Note: **A** Immunofluorescence assessment of the influence of M2pep-Cs-Cur NPs on M2 cell polarization (scale = 25 μm); **B** RT-qPCR analysis of the effect of M2pep-Cs-Cur NPs on M2 cell polarization; **C** Schematic illustration of co-culture of MΦ with MDA-MB-231 and BT-549 cells; (D) CCK8 assay to evaluate the proliferation of MDA-MB-231 and BT-549 cells in each group; **E** Clonogenic assay to assess the proliferation of MDA-MB-231 and BT-549 cells in each group; **F** Transwell assay to determine the invasion of MDA-MB-231 and BT-549 cells in each group (scale = 50 μm); **G** Wound healing test to evaluate the migration of MDA-MB-231 and BT-549 cells in each group (scale = 100 μm); $^{ns}P > 0.05$, $^{*}P < 0.05$, $^{***}P < 0.001$; All cell experiments were conducted in triplicate

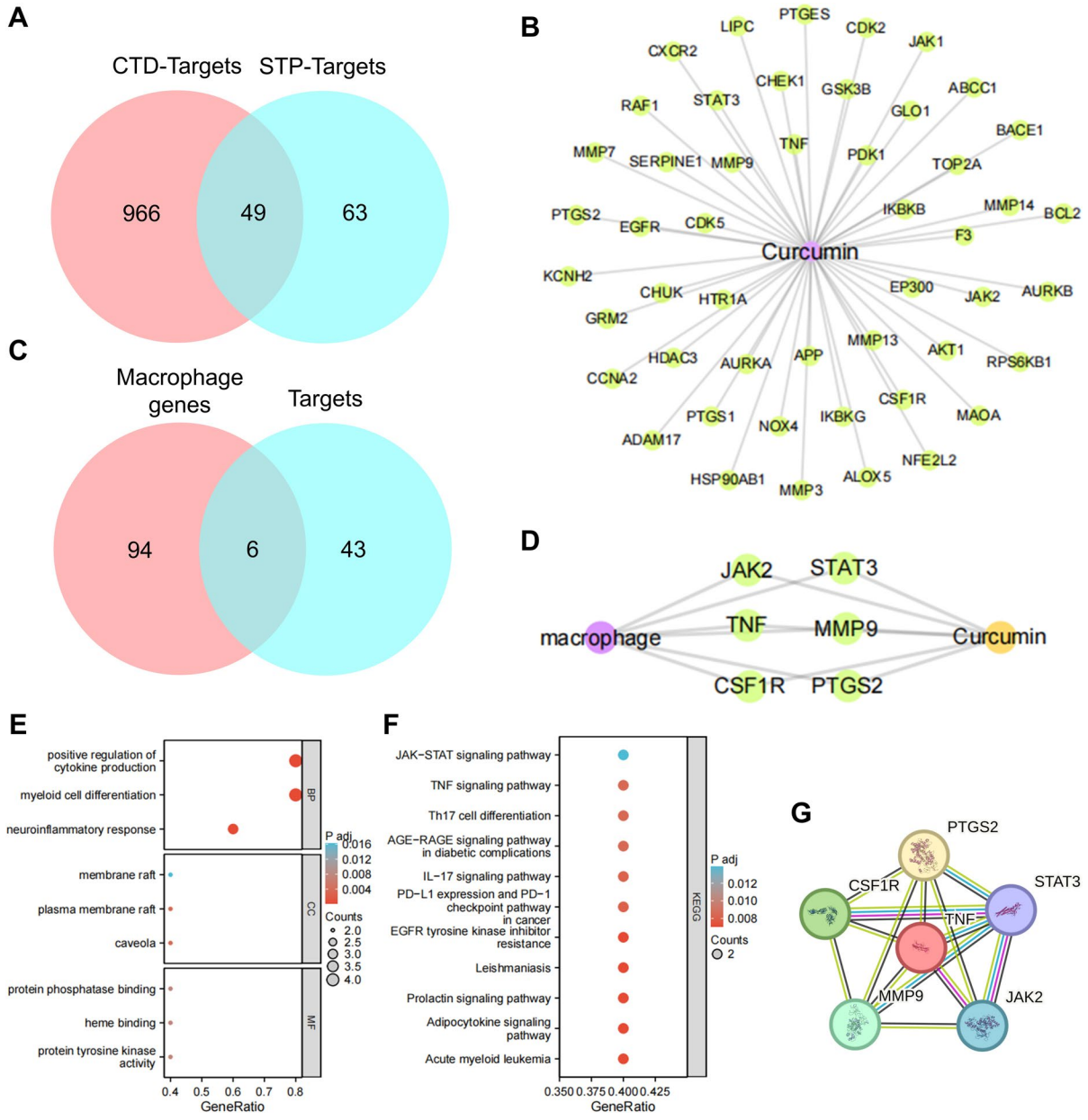

Fig. 4 Bioinformatics analysis reveals the impact of Cur on key genes in TAMs. Note: **A** Venn analysis of Cur target genes from CTD and STP databases; **B** Network diagram of Cur-target genes; **C** Venn analysis of target genes and MΦ-related genes in the GeneCard database; **D** Network diagram of Cur-target genes-MΦ; **E** GO analysis results of six target genes related to MΦ; **F** KEGG analysis results of six target genes related to MΦ; **G** Protein interaction results of six target genes related to MΦ

Cur's 2D and 3D structures were obtained from the PubChem website. The utilization of AutoDockTools 1.5.6 and Vina 1.1.2 software facilitated the molecular docking process of Cur with six proteins (Fig. 5A-B, Table S5). The results revealed the binding free energy of Cur with JAK2 to be −8.2 kcal/mol (Fig. 5C), with STAT3 to be −6.2 kcal/mol (Fig. 5D), with TNF-α to be −6.0 kcal/mol (Fig. 5E), with MMP9 to be −8.9 kcal/mol (Fig. 5F), with CSF1R to be −8.8 kcal/mol (Fig. 5G), and with COX-2 to

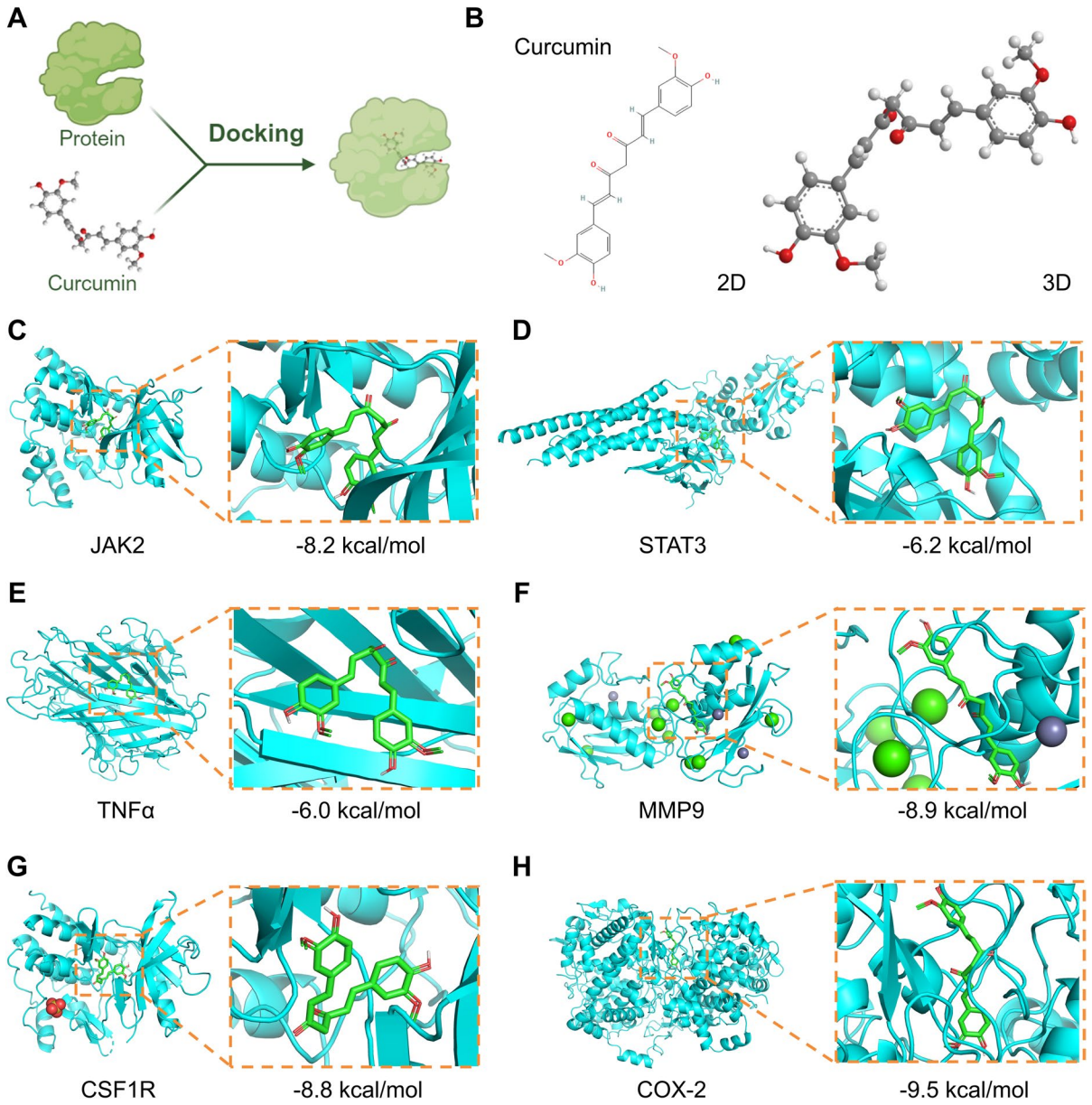

Fig. 5 Molecular docking results of Cur with six target proteins related to MΦ. Note: **A** Schematic illustration of the molecular docking of Cur with target proteins; **B** 2D and 3D structures of Cur molecule; **C** Molecular docking results of Cur with JAK2; **D** Molecular docking results of Cur with STAT3; **E** Molecular docking results of Cur with TNFα; **F** Molecular docking results of Cur with MMP9; **G** Molecular docking results of Cur with CSF1R; **H** Molecular docking results of Cur with COX-2

be −9.5 kcal/mol (Fig. 5H). A binding affinity index of < 0 kcal/mol indicates spontaneous binding and interaction of the molecular proteins, with smaller values suggesting tighter receptor-ligand binding and stronger affinity (Rosa 2021). MD simulations for 100 ns were performed for all six complexes. RMSD analysis indicated that most systems reached equilibrium within the first 20 ns and remained stable, while MMP9 reached equilibrium within 40 ns (Figure S3). Based on stable trajectories (40–100 ns), binding free energy calculations using the MMGB/SA method showed trends consistent with molecular docking

scores. Among these, the Cur-COX-2 complex exhibited the highest binding free energy (−46.0 kcal/mol), indicating the strongest interaction. Details are provided in Table S6. These findings demonstrate that Cur forms stable molecular conformations with JAK2, STAT3, TNF-α, MMP9, CSF1R, and COX-2, with the strongest binding observed for COX-2, primarily mediated by polar interactions (Table S7).

The results above demonstrate that the six key Cur target genes associated with MΦ play crucial roles in regulating the biological processes of cytokine production, myeloid cell differentiation, and inflammatory responses. Additionally, these genes exhibit significant functions in key inflammation-related signaling pathways such as JAK-STAT, TNF, IL-17, and Th17 cell differentiation. Particularly, the tight binding of Cur with COX-2 may be essential in influencing the polarization of TAMs. Cur exhibits the potential to influence MΦ function by modulating specific signaling pathways, as elucidated in this study, offering valuable research directions for further exploration of its anti-inflammatory effects.

M2pep-Cs-Cur NPs modulate TAMs reprogramming via COX-2/TNF&IL-17 pathways

To further investigate whether M2pep-Cs-Cur NPs impact TAM reprogramming through the regulation of COX-2, we examined the expression of COX-2 in untreated and treated M2 cells with M2pep-Cs-Cur NPs. The data reveals a considerable drop in both COX-2 mRNA and protein expression in M2 cells treated with M2pep-Cs-Cur NPs in contrast with the untreated group (Fig. 6A-B). The IL-17 and TNF signaling pathways were found to be enriched with COX-2, as revealed by KEGG analysis (Table S4). Therefore, we also assessed the protein expression levels of IL-17 and TNF-α in untreated and treated M2 cells with NPs. The results indicate an upregulation of IL-17 and TNF-α protein expression levels in M2 cells treated with M2pep-Cs-Cur NPs (Fig. 6C).

In the follow-up experiment, we conducted COX-2 overexpression in M2 cells treated with M2pep-Cs-Cur NPs (referred to as NPs + oe-COX-2, as shown in Fig. 6D-E) to evaluate the influence of COX-2 overexpression on the reprogramming of M2 cells treated with M2pep-Cs-Cur NPs. The examination findings exhibited that when juxtaposed with the NPs + oe-NC group, M2 cells overexpressing COX-2 displayed significantly enhanced fluorescence intensity of the M2 cell marker CD163, while the fluorescence intensity of the M1 cell marker CD86 was reduced (Fig. 6F). Consistent with the immunofluorescence findings, RT-qPCR results demonstrated upregulation of the M2 cell markers CD163 and IL-10 expression, and downregulation of the M1 cell markers CD80, CD86, and IL-1β expression (Fig. 6G). These results suggest that M2pep-Cs-Cur NPs may induce the reprogramming of M2 cells by suppressing COX-2 expression.

To further investigate the effect of M2pep-Cs-Cur NPs on the reprogramming of M2 cells and their impact on the growth and invasion of TNBC cells by suppressing COX-2 expression, we co-cultured oe-NC or oe-COX-2 M2 cells treated with M2pep-Cs-Cur NPs with MDA-MB-231 and BT-549 cells. Results from the EdU labeling and colony formation experiments indicated that under M2pep-Cs-Cur NPs treatment, MDA-MB-231 and BT-549 cell proliferation was enhanced when co-cultured with M2 cells overexpressing COX-2 relative to the NPs + oe-NC group (Fig. 6H-I). Additionally, Transwell and migration assay results revealed that under M2pep-Cs-Cur NPs treatment, co-culturing MDA-MB-231 and BT-549 cells with oe-COX-2 M2 cells enhanced their invasion and migration capabilities contrasted against the NPs + oe-NC group (Fig. 6J-K).

These outcomes illustrate that M2pep-Cs-Cur NPs induce the reprogramming of M2 cells by inhibiting COX-2 expression, thereby suppressing the growth and invasion of TNBC cells.

M2pep-Cs-Cur NPs suppress TNBC growth and invasion while enhancing anti-PD-L1 immunotherapy efficacy

Investigating the in vivo impact of M2pep-Cs-Cur NPs on TAMs repolarization, TNBC proliferation, invasion, and anti-PD-L1 immunomodulation, a murine model involving orthotopic transplantation of 4T1 cells was created, with subsequent administration of M2pep-Cs-Cur NPs or anti-PD-L1 therapy to the animal subjects. The allocation of mice was random, leading them to be grouped into the Control group, M2pep-Cs-Cur NPs treatment group, and M2pep-Cs-Cur NPs combined with the anti-PD-L1 treatment group.

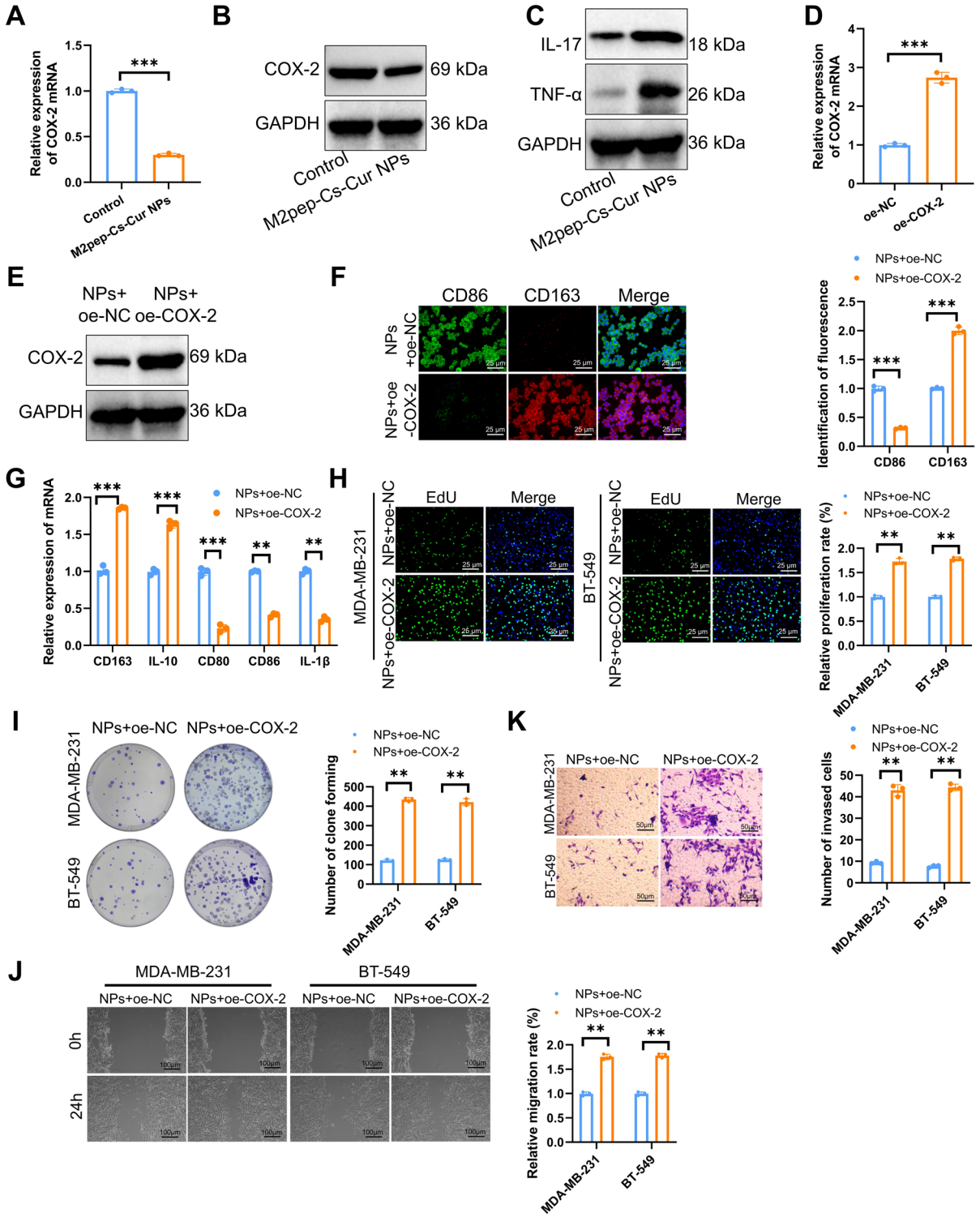
A
Relative expression of COX-2 mRNA
***
Control
M2pep-Cs-Cur NPs
B
COX-2
69 kDa
GAPDH
36 kDa
Control
M2pep-Cs-Cur NPs
C
IL-17
18 kDa
TNF-α
26 kDa
GAPDH
36 kDa
Control
M2pep-Cs-Cur NPs
D
Relative expression of COX-2 mRNA
***
oe-NC
oe-COX-2
E
NPs+ oe-NC
NPs+ oe-COX-2
COX-2
69 kDa
GAPDH
36 kDa
F
CD86
CD163
Merge
NPs +oe-NC
NPs+oe -COX-2
25 μm
NPs+oe-NC
NPs+oe-COX-2
Identification of fluorescence
***
***
CD86
CD163
G
Relative expression of mRNA
***
***
***
**
**
NPs+oe-NC
NPs+oe-COX-2
CD163
IL-10
CD80
CD86
IL-1β
H
MDA-MB-231
BT-549
NPs+oe-NC
NPs+oe-COX-2
EdU
Merge
25 μm
NPs+oe-NC
NPs+oe-COX-2
Relative proliferation rate (%)
**
**
MDA-MB-231
BT-549
I
NPs+oe-NC
NPs+oe-COX-2
MDA-MB-231
BT-549
Number of clone forming
**
**
MDA-MB-231
BT-549
K
MDA-MB-231
BT-549
NPs+oe-NC
NPs+oe-COX-2
50μm
Number of invased cells
**
**
MDA-MB-231
BT-549
J
MDA-MB-231
BT-549
NPs+oe-NC
NPs+oe-COX-2
0h
24h
100μm
Relative migration rate (%)
**
**
MDA-MB-231
BT-549

◂**Fig. 6** Impact of M2pep-Cs-Cur NPs on TAMs reprogramming through COX-2/TNF&IL-17 pathway. Note: **A** Expression of COX-2 mRNA in untreated and treated M2 cells with M2pep-Cs-Cur NPs; **B** Expression of COX-2 protein in untreated and treated M2 cells with M2pep-Cs-Cur NPs; **C** Protein expression of IL-17 and TNF-α in untreated and treated M2 cells with M2pep-Cs-Cur NPs; **D** Validation of COX-2 overexpression at mRNA level; **E** Validation of COX-2 overexpression at protein level; **F** Immunofluorescence staining of M1 and M2 markers in different groups of MΦ (scale bar = 25 μm); **G** RT-qPCR analysis of M1 and M2 markers in different groups of MΦ; **H** EdU labeling experiment to assess the proliferation of MDA-MB-231 and BT-549 cells co-cultured with MΦ in different groups (scale bar = 25 μm); **I** Clonogenic assay to evaluate the proliferation of MDA-MB-231 and BT-549 cells co-cultured with MΦ in different groups; **J** Scratch wound assay of MDA-MB-231 and BT-549 cells co-cultured with MΦ, evaluating migration (scale bar = 100 μm); **K** Transwell assay of MDA-MB-231 and BT-549 cells co-cultured with MΦ, assessing invasion (scale bar = 50 μm); $^{*}P < 0.05$, $^{**}P < 0.01$, $^{***}P < 0.001$; All cellular experiments were performed in triplicate

Initially, we assessed the tumor weights in the mice to evaluate tumor growth. The data depicted a notable drop in the weight of allograft tumors in the M2pep-Cs-Cur NPs treatment group contrasted with the Control group, with further tumor growth inhibition observed in the combined treatment group with anti-PD-L1 (Fig. 7A). Immunohistochemical analysis revealed decreased expression of Ki67 and PCNA in allograft tumors following treatment with M2pep-Cs-Cur NPs or combined treatment with anti-PD-L1 (Fig. 7B). These findings suggest that M2pep-Cs-Cur NP treatment suppressed in vivo proliferation of allograft TNBC cells, with a more pronounced inhibitory effect observed in combination with anti-PD-L1 therapy.

Subsequent to the treatment with M2pep-Cs-Cur NPs, the MΦ reprogramming status in TNBC grafts was assessed through flow cytometry. The results revealed an escalation in M1 cells marked by CD80 and CD86 and a downturn in M2 cells marked by CD163 and CD206 in allograft tumors in both the M2pep-Cs-Cur NPs treatment group and the combination therapy group, in contrast with the Control group (Fig. 7C). Additionally, Western blot analysis exhibited downregulation of COX-2 expression and an upregulation of IL-17 and TNFα expression in allograft tumors in the M2pep-Cs-Cur NPs treatment group and the combination therapy group, in relation to the Control group (Fig. 7D).

Lastly, we conducted a safety evaluation of the in vivo biocompatibility of M2pep-Cs-Cur NPs. The results demonstrated a steady increase in body weight of all treated mice, with no signs of discomfort or mortality (Fig. 7E). Analysis of heart, liver, spleen, lung, and kidney samples in every grouping revealed no apparent damage in the H&E-stained sections upon microscopic scrutiny (Fig. 7F). Moreover, serum biochemical analysis indicated no significant differences in liver function indicators (ALT, AST), cardiac function indicators (CK, LDH), and kidney function indicators (CREA, urea) among the groups (Fig. 7G-I).

These findings suggest that M2pep-Cs-Cur NPs exhibit a high safety profile, suppress the formation of tumor-promoting M2-like MΦ in the TNBC TME, promote TAMs reprogramming, inhibit TNBC tumor progression, and enhance the efficacy of anti-PD-L1 treatment.

Transcriptome sequencing reveals key pathway alterations in TAMs reprogramming targeted by M2pep-Cs-Cur NPs

To further elucidate the molecular mechanisms by which M2pep-Cs-Cur NPs induce TAMs reprogramming in vivo, we conducted whole transcriptome sequencing analysis on MΦ extracted from the allograft tumors of the same batch of mice from the Control group and the M2pep-Cs-Cur NPs treatment group (Fig. 8A).

When contrasted with the Control group, a sum of 737 DEGs was identified in the M2pep-Cs-Cur NPs group, with 303 genes in an upregulated state and 434 genes noted as downregulated (Fig. 8B). Subsequently, the DEGs underwent enrichment analyses through GO and KEGG pathways to gain further insights. GO enrichment analysis indicated a remarkable enrichment of DEGs in biological processes (BP) related to white blood cell migration, regulation of inflammatory responses, and positive regulation of the cell cycle. This emphasizes the crucial role of MΦ in immune response and cell proliferation. In terms of cellular components (CC), gene enrichment was observed in locations such as the receptor complex, cell leading edge, and spindle apparatus, possibly associated with the recognition, positioning, and division functions of MΦ. The molecular function

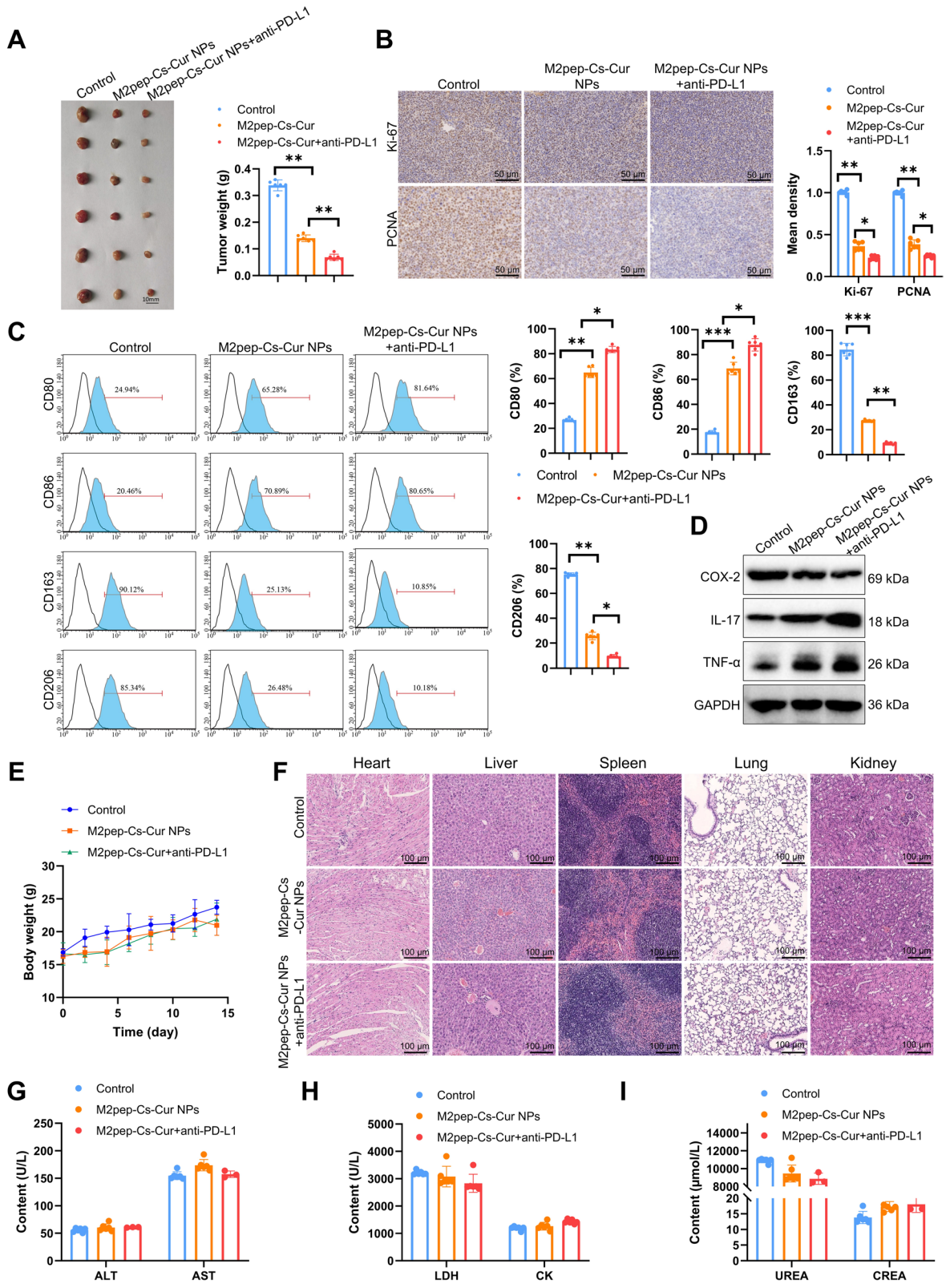
A
Control
M2pep-Cs-Cur NPs
M2pep-Cs-Cur NPs+anti-PD-L1
Control
M2pep-Cs-Cur
M2pep-Cs-Cur+anti-PD-L1
Tumor weight (g)
B
Control
M2pep-Cs-Cur NPs
M2pep-Cs-Cur NPs +anti-PD-L1
Ki-67
PCNA
50 μm
Control
M2pep-Cs-Cur
M2pep-Cs-Cur +anti-PD-L1
Mean density
Ki-67
PCNA
C
Control
M2pep-Cs-Cur NPs
M2pep-Cs-Cur NPs +anti-PD-L1
CD80
CD86
CD163
CD206
24.94%
65.28%
81.64%
20.46%
70.89%
80.65%
90.12%
25.13%
10.85%
85.34%
26.48%
10.18%
CD80 (%)
CD86 (%)
CD163 (%)
CD206 (%)
Control
M2pep-Cs-Cur NPs
M2pep-Cs-Cur+anti-PD-L1
D
Control
M2pep-Cs-Cur NPs
M2pep-Cs-Cur NPs +anti-PD-L1
COX-2
IL-17
TNF-α
GAPDH
69 kDa
18 kDa
26 kDa
36 kDa
E
Control
M2pep-Cs-Cur NPs
M2pep-Cs-Cur+anti-PD-L1
Body weight (g)
Time (day)
F
Heart
Liver
Spleen
Lung
Kidney
Control
M2pep-Cs -Cur NPs
M2pep-Cs-Cur NPs +anti-PD-L1
100 μm
G
Control
M2pep-Cs-Cur NPs
M2pep-Cs-Cur+anti-PD-L1
Content (U/L)
ALT
AST
H
Control
M2pep-Cs-Cur NPs
M2pep-Cs-Cur+anti-PD-L1
Content (U/L)
LDH
CK
I
Control
M2pep-Cs-Cur NPs
M2pep-Cs-Cur+anti-PD-L1
Content (μmol/L)
UREA
CREA

◂**Fig. 7** M2pep-Cs-Cur NPs induce TAMs reprogramming to suppress TNBC growth, invasion, and immunoresistance. Note: **A** Tumor weight changes in each group of mice; **B** Immunohistochemical detection of Ki-67 and PCNA expression in tumor tissues (scale = 50 μm); **C** Flow cytometric analysis of MΦ M1 and M2 markers in tumors; **D** Expression detection of COX-2, IL-17, and TNFα in tumor tissues of each group of mice; **E** Changes in body weight of mice in each group; **F** H&E staining results of heart, liver, spleen, lungs, and kidneys in each group of mice (scale = 100 μm); **G** Evaluation of liver function indicators (ALT, AST) in each group of mice; **H** Assessment of cardiac function indicators (CK, LDH) in each group of mice; **I** Examination of renal function indicators (CREA, urea) in each group; $^{*}P < 0.05$, $^{**}P < 0.01$, $^{***}P < 0.001$; $n = 6$ for each group

(MF) analysis indicated significant enrichment of DEGs in activities such as protein binding, cytokine binding, and oxidoreductase activity, particularly enzymes acting on the CH-CH group with NAD or NADP as cofactors, potentially involving energy metabolism and cell signaling pathways (Fig. 8C). KEGG enrichment analysis highlighted that the DEGs in MΦ are primarily linked to signaling pathways involved in tumorigenesis, immune response, and cell cycle regulation. Notably, the enrichment of pathways related to tumorigenesis transcriptional misregulation underscores the pivotal role that MΦ may play in cancer development. Furthermore, the enrichment of pathways like apoptosis and the TNF signaling pathway reveals the potential importance of MΦ in immune regulation and metabolic control (Fig. 8D). Additionally, based on the sequencing results, the application of M2pep-Cs-Cur NPs resulted in the reduction of COX-2 gene expression and promoted the shift of TAMs from M2 to M1 phenotype, which was later confirmed (Fig. 8E-F).

In summary, transcriptional analysis of mouse TAMs treated with M2pep-Cs-Cur NPs revealed 737 DEGs, with gene functions related to immune response and inflammation regulation being enriched. The analysis results indicate that the treatment enhances the crucial roles of MΦ in cell cycle regulation and metabolic control, suggesting potential anti-tumor mechanisms. Furthermore, treatment with M2pep-Cs-Cur NPs led to the downregulation of COX-2 gene expression, confirming their ability to induce the transition of TAMs from the M2 to the M1 phenotype. These findings provide molecular evidence for NP-mediated TAM reprogramming.

Discussion

TNBC is recognized as an exceptionally aggressive cancer subtype with restricted treatment choices compared to other breast cancer types, leading to a dismal prognosis (Lee et al. 2021). Within the TME of TNBC, MΦ, also known as TAMs, play a critical role (Pal et al. 2021; Wang et al. 2021a, b, c; Li et al. 2022a, b, c, d). Research has demonstrated that the M2 phenotype of TAMs is significantly linked to cancer progression, spread, and evasion of the immune system (Chen et al. 2022a, b, c; Ji et al. 2022; Zhang et al. 2023a, b, c, d). However, traditional treatment strategies often overlook these cells in the microenvironment. Therefore, the development of new strategies, particularly focusing on modulating the polarization state of TAMs to treat TNBC, is crucial (Pu and Ji 2022, Li et al. 2022a, b, c, d; Tang et al. 2023). Although Cur has shown immunomodulatory potential, its application in targeting TAMs in TNBC remains underexplored. Moreover, clinical use of Cur is limited by its low solubility and bioavailability (Hafez Ghoran et al. 2022). This study demonstrates a novel approach to inhibit tumor growth by reprogramming M2-type TAMs through an NP delivery system designed to target these specific cells within the TME.

The M2pep-Cs-Cur NPs used in this study were designed as a Cs-based carrier system incorporating a specific targeting peptide (M2pep) and Cur (Han et al. 2023, 2021). This design ensures efficient drug loading and stable release, while the incorporation of M2pep allows the NPs to specifically target M2-polarized TAMs. Compared to earlier research studies focusing on Cur's effects on MΦ polarization and associated diseases, this approach demonstrates superior specificity and targeting efficiency (Bai et al. 2016, Guo et al. 2023a, b, Huang et al. 2024) (Fig. 9). In comparison to traditional anti-tumor treatments, this strategy minimizes toxicity to normal tissue cells while enhancing anti-tumor efficacy. Unlike conventional approaches that directly target tumor cells using immune modulators or small molecules, this study employs modulation of immune cells within the TME, offering a novel strategy for TNBC treatment. Moreover, the pH-sensitive properties of the NPs enable effective drug release in the acidic TME, surpassing the limitations of traditional therapies. This specificity allows the M2pep-Cs-Cur NPs to reprogram

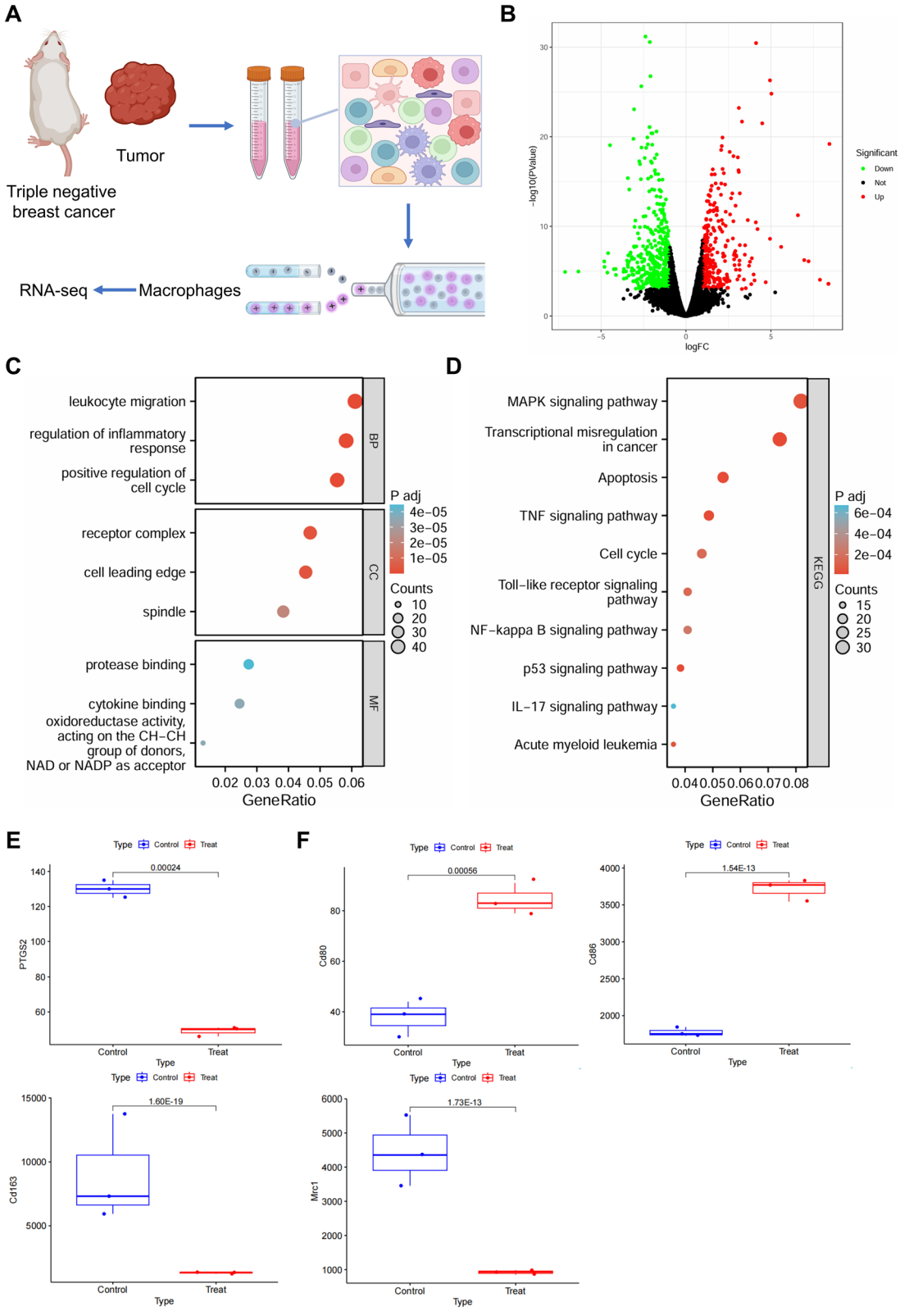
A
Tumor
Triple negative breast cancer
RNA-seq
Macrophages
B
-log10(PValue)
logFC
Significant
Down
Not
Up
C
leukocyte migration
regulation of inflammatory response
positive regulation of cell cycle
receptor complex
cell leading edge
spindle
protease binding
cytokine binding
oxidoreductase activity, acting on the CH-CH group of donors, NAD or NADP as acceptor
BP
CC
MF
P adj
Counts
GeneRatio
D
MAPK signaling pathway
Transcriptional misregulation in cancer
Apoptosis
TNF signaling pathway
Cell cycle
Toll-like receptor signaling pathway
NF-kappa B signaling pathway
p53 signaling pathway
IL-17 signaling pathway
Acute myeloid leukemia
KEGG
E
PTGS2
Cd163
F
Cd80
Cd86
Mrc1
Type
Control
Treat

◂**Fig. 8** Transcriptomic sequencing reveals key pathway changes in M2pep-Cs-Cur NPs targeting TAMs reprogramming. Note: **A** Schematic overview of transcriptomic sequencing in TNBC mouse tissues; **B** Volcano plot analysis of DGEs in untreated (Control, $n=3$) and treated (Treat, $n=3$) groups with M2pep-Cs-Cur NPs, with red dots indicating significantly upregulated genes, green dots representing significantly downregulated genes, and black dots denoting genes with no significant difference; **C** Bubble chart for DEGs GO analysis; **D** Bubble chart for DEGs KEGG analysis; **E** Expression levels of COX-2 gene in transcriptomic sequencing data; **F** Expression levels of genes related to MΦ M1 and M2 phenotypes in transcriptomic sequencing data; $n=3$ for each group

the polarization of MΦ in the TME, thus modulating the distribution of immune cells and enhancing the effectiveness of anti-PD-L1 medications. The combination of M2pep-Cs-Cur NPs with anti-PD-L1 antibodies pointed out synergistic effects in suppressing tumor growth and immune evasion. This combination therapy not only strengthened the immune response against tumors but also remodeled the TME by altering TAM polarization. Compared to single-modality treatments reported in other studies (Abdou et al. 2022; Liu et al. 2023), this approach showed significantly enhanced therapeutic potential.

COX-2 is responsible for producing prostaglandins such as prostaglandin E2 (PGE2), which are released into the TME by M2-polarized MΦ. These prostaglandins promote resistance to apoptosis, invasion, metastasis, and immune evasion in tumor cells (Hashemi Goradel et al. 2018). By utilizing bioinformatics tools, this study not only identified key genes, such as COX-2, through which Cur influences the polarization of TAMs, but also revealed the direct interaction between Cur and these genes using molecular docking techniques. Implementing this approach has broadened our comprehension regarding the process of medication impact and enhanced the accuracy of specialized treatment. Furthermore, this approach indicates that by integrating traditional pharmacological research with modern bioinformatics methods, a more comprehensive exploration and validation of the potential mechanisms of new drugs can be achieved.

In TNBC, the growth, invasion, and immune escape of tumors are boosted by M2-polarized TAMs which secrete cytokines including IL-10 and TGF-β. These factors facilitate immune surveillance evasion, angiogenesis, and resistance to therapies within the TME (Liu et al. 2024; Huo et al. 2022). Studies have shown that reprogramming TAMs from the M2 to the M1 phenotype can effectively suppress tumor growth and invasion (Fernando et al. 2023). The immune system's capacity to identify and remove tumor cells is heightened by M1 MΦ, which secrete pro-inflammatory cytokines including IL-12 and TNF-α (Ren et al. 2024). The IL-17 as well as TNF signal pathways are crucial in driving the transition of MΦ towards the M1 phenotype through stimulation of the generation of inflammatory agents (Schinocca et al. 2021; Wang et al. 2022a, b, c). Developing therapeutic strategies that facilitate this reprogramming has become a key focus in TNBC research (Bill et al. 2023; Hao et al. 2022; Wang et al. 2022a, b, c). This approach not only provides an alternative to overcome drug resistance in traditional treatments but also improves immune-mediated tumor clearance. In this study, in vivo experiments demonstrated that M2pep-Cs-Cur NPs effectively induced M2 MΦ reprogramming. When combined with anti-PD-L1 therapy, the NPs exhibited a strong synergistic effect (Fig. 7A-B), enhancing the efficacy of PD-L1 blockade and potentially addressing PD-L1 resistance. The integration approach could hold substantial implications in enhancing the survival rates and lifestyle quality for individuals with TNBC in upcoming clinical scenarios. Therefore, novel scientific perspectives are provided in this investigation as it explains the involvement of TAMs in tumor advancement, while also proposing innovative therapeutic objectives and methodologies for treatment-resistant TNBC in clinical scenarios.

While the results of this study are encouraging, there are some limitations to consider. First, the study utilized a TNBC xenograft mouse model, which, although to some extent, can simulate human disease, still lacks the complexity of human TNBC, thus requiring further validation of its clinical relevance in human studies. Secondly, although NPs have demonstrated good targetability and efficacy, the biological safety implications over an extended period and the likelihood of immune reactions have not been sufficiently researched. Moreover, the high production costs and technical requirements of NPs may impact their feasibility for widespread clinical applications. In this study, glutaraldehyde was used as a crosslinker during Cs NP preparation based on previous literature (Zhou et al. 2014). Although no significant tissue toxicity was observed in short-term experiments, this might be attributed to the low dose and short duration. Future clinical applications will

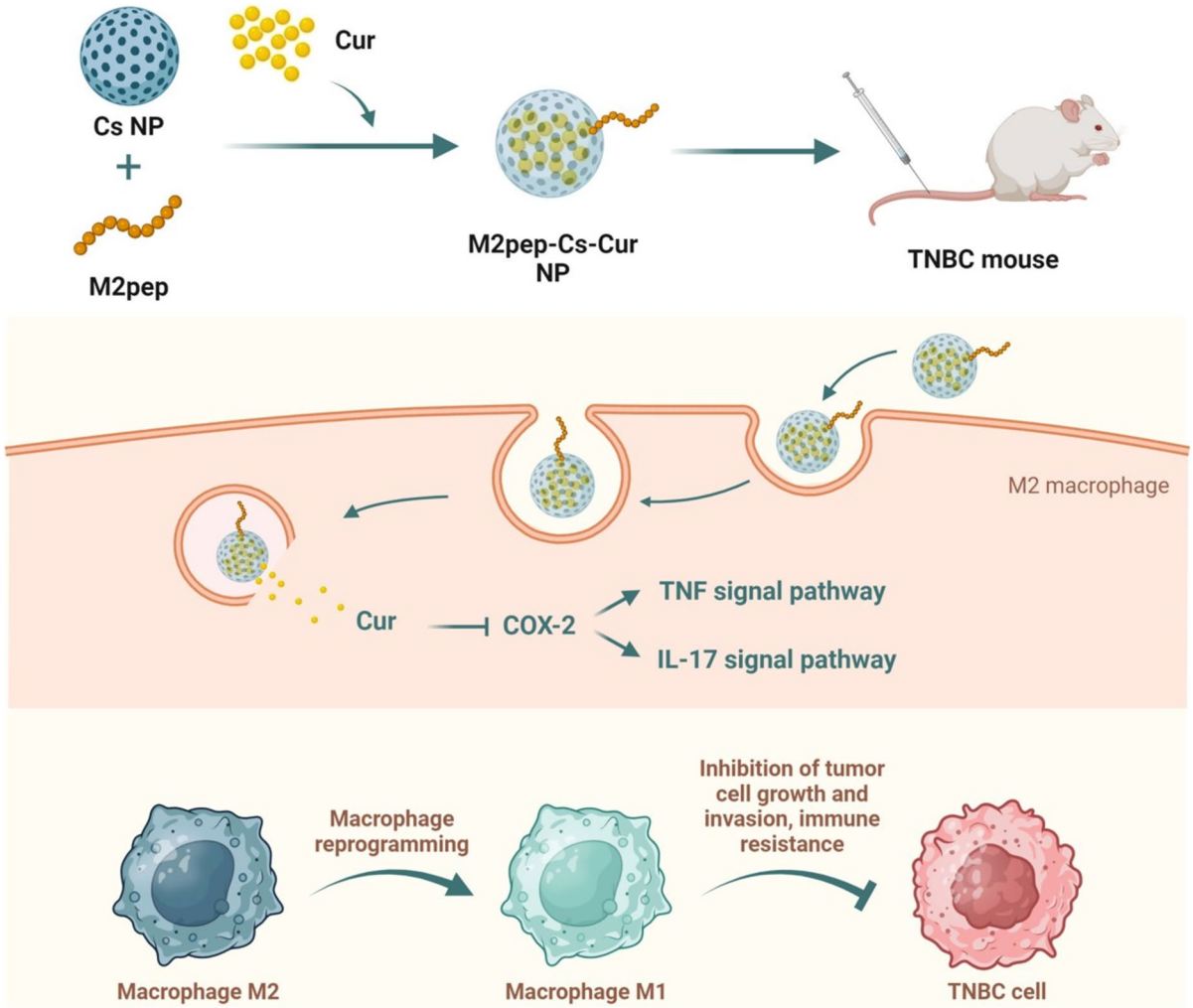

Fig. 9 M2pep-Cs-Cur NPs target COX-2 to reverse TAMs M2 polarization and inhibit immunotherapy resistance in TNBC

require the optimization of crosslinking methods. Literature has reported that Cs/lecithin NPs are ideal carriers for hydrophilic and hydrophobic compounds, capable of enhancing anti-tumor activity through encapsulation via electrostatic interactions (Rafiee and Rezaee 2021; Ning et al. 2023). The development of Cur-loaded Cs/lecithin NPs using self-assembly techniques (Yu et al. 2024) may serve as a potential direction for optimizing future drug designs. Further optimization of synthesis conditions, such as the conjugation time of M2pep, is also necessary, as prolonged coupling may affect M2pep activity. Alternative methods, such as the "Michael addition reaction at RT for 4 h" (Zhang et al. 2023a, b, c, d), could be explored for M2pep coupling. Finally, the high production cost and technical requirements of NP synthesis could limit their feasibility for widespread clinical use. Future research should focus on cost-effective methods to enable broader application.

Ahead research has a responsibility to tackle the shortcomings of the current examination through structuring clinical experiments aimed at confirming the efficacy and safety of this pioneering NP therapy in patients with TNBC. Additionally, research should aim to further optimize the design of NPs, enhancing their stability and biocompatibility while reducing potential side effects. Furthermore, exploring the possibilities of combining this therapy with other treatment modalities, such as radiotherapy and chemotherapy, as well as investigating similar mechanisms of

TAM polarization in different tumor types, may open up broader applications in treatment. Through these studies, enhanced understanding and strategic utilization of the TME in cancer therapy can significantly elevate treatment efficacy, providing a ray of hope for cancer patients.

Conclusion

This study successfully developed M2pep-Cs-Cur NPs, a novel targeted delivery system that effectively reprograms TAMs from an M2 to M1 phenotype in the TME of TNBC. The NPs demonstrated significant anti-tumor effects, encompassing the hindrance of TNBC cell proliferation, migration, and invasion, as well as enhancement of sensitivity to anti-PD-L1 therapy in both in vitro and in vivo models. Through bioinformatics analysis and molecular docking, COX-2 was identified as a critical target of Cur, influencing TAM reprogramming via the TNF and IL-17 pathways. This study not only provides a promising therapeutic strategy to overcome immunotherapy resistance in TNBC but also highlights the potential of nanotechnology-based approaches to advance cancer treatment by targeting the TME.

Author contributions Xiaoshen Dong and Xiaoou Wang: Contributed equally to the experimental design, data acquisition, and analysis. Drafted the manuscript. Xinyu Zheng: Conducted bioinformatics analysis and assisted with experimental validation. Haiyang Jiang: Provided technical support for nanoparticle synthesis and characterization. Lu Liu: Assisted in conducting in vitro and in vivo experiments and contributed to data interpretation. Ningye Ma: Supervised the project, contributed to experimental design, and provided clinical insights into TNBC therapy. Shuo Wang: Conceived the study, supervised the project, and critically revised the manuscript. All authors have reviewed and approved the final manuscript.

Funding This work was supported by grants from the Natural Science Foundation of Liaoning Province (grant no. 2023-MS-175 and 2024-MS-023).

Data availability The datasets used or analyzed during the current study are available from the corresponding author on reasonable request.

Declarations

Ethical statement All animal experiments were approved by the Animal Ethics Committee of China Medical University (No. CMUKT20240259).

Competing interests The authors declare no competing interests.

References

Abdou Y, Goudarzi A, Yu JX, Upadhaya S, Vincent B, Carey LA. Immunotherapy in triple negative breast cancer: beyond checkpoint inhibitors [Internet]. npj Breast Cancer. Springer Science and Business Media LLC. 2022. [cited 2025 Jan 16]. Available from: https://doi.org/10.1038/s41523-022-00486-y.

Aghbashlo M, Amiri H, Moosavi Basri SM, Rastegari H, Lam SS, Pan J, et al. Tuning chitosan's chemical structure for enhanced biological functions [Internet]. Trends in Biotechnology. Elsevier BV. 2023; pp 785–97. [cited 2025 Jan 16]. Available from: https://doi.org/10.1016/j.tibtech.2022.11.009.

Asadollahi L, Mahoutforoush A, Dorreyatim SS, Soltanfam T, Paiva-Santos AC, Peixoto D, et al. Co-Delivery of erlotinib and resveratrol via nanostructured lipid Carriers: A synergistically promising approach for cell proliferation prevention and ROS-Mediated apoptosis activation [Internet]. International Journal of Pharmaceutics. Elsevier BV. 2022; p 122027 [cited 2025 Jan 16]. Available from: https://doi.org/10.1016/j.ijpharm.2022.122027.

Bai X, Oberley-Deegan RE, Bai A, Ovrutsky AR, Kinney WH, Weaver M, et al. Curcumin enhances human macrophage control of Mycobacterium tuberculosis infection [Internet]. Respirology. Wiley. 2016, pp 951–7 [cited 2025 Jan 16]. Available from: https://doi.org/10.1111/resp.12762.

Barkal AA, Brewer RE, Markovic M, Kowarsky M, Barkal SA, Zaro BW, et al. CD24 signalling through macrophage Siglec-10 is a target for cancer immunotherapy [Internet]. Nature. Springer Science and Business Media LLC. 2019; pp 392–6 [cited 2025 Jan 16]. Available from: https://doi.org/10.1038/s41586-019-1456-0.

Bill R, Wirapati P, Messemaker M, Roh W, Zitti B, Duval F, et al. CXCL9:SPP1 macrophage polarity identifies a network of cellular programs that control human

cancers [Internet]. Science. American Association for the Advancement of Science (AAAS). 2023; pp 515–24 [cited 2025 Jan 16]. Available from: https://doi.org/10.1126/science.ade2292.

Chen B, Song Y, Zhan Y, Zhou S, Ke J, Ao W, et al. Fangchinoline inhibits non-small cell lung cancer metastasis by reversing epithelial-mesenchymal transition and suppressing the cytosolic ROS-related Akt-mTOR signaling pathway [Internet]. Cancer Letters. Elsevier BV. 2022a; pp 215783 [cited 2025 Jan 16]. Available from: https://doi.org/10.1016/j.canlet.2022.215783.

Chen X, Yang M, Yin J, Li P, Zeng S, Zheng G, et al. Tumor-associated macrophages promote epithelial–mesenchymal transition and the cancer stem cell properties in triple-negative breast cancer through CCL2/AKT/β-catenin signaling [Internet]. Cell Commun Signal. Springer Science and Business Media LLC. 2022c. [cited 2025 Jan 16]. Available from: https://doi.org/10.1186/s12964-022-00888-2.

Chen Y, Su Y, Pang X, Song X, Zhao W, Yu M. Synthesis and Evaluation of Technetium-99m-Labeled pH (Low) Insertion Peptide Variant 7 for Early Diagnosis of MDA-MB-231 Triple-Negative Breast Cancer by Targeting the Tumor Microenvironment [Internet]. Front. Oncol. Frontiers Media SA. 2022d. [cited 2025 Jan 16]. Available from: https://doi.org/10.3389/fonc.2022.869260.

Cortes J, Rugo HS, Cescon DW, Im S-A, Yusof MM, Gallardo C, et al. Pembrolizumab plus Chemotherapy in Advanced Triple-Negative Breast Cancer [Internet]. N Engl J Med. Massachusetts Medical Society. 2022; pp 217–26 [cited 2025 Jan 16]. Available from: https://doi.org/10.1056/nejmoa2202809.

Darvishi S, Hosseinzadeh H, Kazeminava F, Mahoutforoush A, Tajik M, Rasoulzadehzali M, et al. Heparin-functionalized Cu-based metal-organic framework: An efficient active and passive targeting nanocarrier for anticancer doxorubicin drug delivery [Internet]. International Journal of Biological Macromolecules. Elsevier BV. 2024; p 136648 [cited 2025 Jan 16]. Available from: https://doi.org/10.1016/j.ijbiomac.2024.136648.

Dass SA, Tan KL, Selva Rajan R, Mokhtar NF, Mohd Adzmi ER, Wan Abdul Rahman WF, et al. Triple Negative Breast Cancer: A Review of Present and Future Diagnostic Modalities [Internet]. Medicina. MDPI AG. 2021; p 62. [cited 2025 Jan 16] Available from: https://doi.org/10.3390/medicina57010062.

Datta I, Bangi E. Senescent cells and macrophages cooperate through a multi-kinase signaling network to promote intestinal transformation in Drosophila [Internet]. Cold Spring Harbor Laboratory. 2023. [cited 2025 Jan 16]. Available from: https://doi.org/10.1101/2023.05.15.540869.

Deng S, Gu J, Jiang Z, Cao Y, Mao F, Xue Y, et al. Application of nanotechnology in the early diagnosis and comprehensive treatment of gastrointestinal cancer [Internet]. J Nanobiotechnol. Springer Science and Business Media LLC. 2022. [cited 2025 Jan 16]. Available from: https://doi.org/10.1186/s12951-022-01613-4.

Derakhshan F, Reis-Filho JS. Pathogenesis of triple-negative breast cancer [Internet]. Annu Rev Pathol Mech Dis. 2022;17:181–204. https://doi.org/10.1146/annurev-pathol-042420-093238. [cited 2025 Jan 16].

Fernando V, Zheng X, Sharma V, Furuta S. Reprogramming of breast tumor-associated macrophages with modulation of arginine metabolism [Internet]. Cold Spring Harbor Laboratory. 2023. [cited 2025 Jan 16]. Available from: https://doi.org/10.1101/2023.08.22.554238.

Gao S, Zhou J, Liu N, Wang L, Gao Q, Wu Y, et al. Curcumin induces M2 macrophage polarization by secretion IL-4 and/or IL-13 [Internet]. J Mol Cell Cardiol. 2015;85:131–9. https://doi.org/10.1016/j.yjmcc.2015.04.025. Elsevier BV, [cited 2025 Jan 16].

Gao J, Xia L, Jia Z, Zhang J, Song M, Ding W, Li L, Liang X. Chitosan regulates CAV1 to facilitate M2 macrophage differentiation through activation of canonical Wnt signaling pathway in diabetic skin trauma model rats. J Biol Regul Homeost Agents [Internet]. 2023;37(8):4335–43. https://doi.org/10.23812/j.biol.regul.homeost.agents.20233708.424.

Guo P, Ibrahim MAA, Zhang H, et al. Curcumin mediates macrophage polarization to inhibit the formation of abdominal aortic aneurysms by inhibiting the expression of histone acetyltransferase EP300. Arab J Chem. 2023a;16(11):105227. https://doi.org/10.1016/j.arabjc.2023.105227. [Internet].

Guo S, Liu X, Zhang J, Huang Z, Ye P, Shi J, et al. Integrated analysis of single-cell RNA-seq and bulk RNA-seq unravels T cell-related prognostic risk model and tumor immune microenvironment modulation in triple-negative breast cancer [Internet]. Comput Biol Med. Elsevier BV. 2023b; 107066 [cited 2025 Jan 16]. Available from: https://doi.org/10.1016/j.compbiomed.2023.107066.

Hafez Ghoran S, Calcaterra A, Abbasi M, Taktaz F, Nieselt K, Babaei E. Curcumin-based nanoformulations: a promising adjuvant towards cancer treatment [Internet]. Molecules. MDPI AG. 2022; 5236 [cited 2025 Jan 16]. Available from: https://doi.org/10.3390/molecules27165236.

Han S, Wang W, Wang S, Yang T, Zhang G, Wang D, et al. Tumor microenvironment remodeling and tumor therapy based on M2-like tumor associated macrophage-targeting nano-complexes [Internet]. Theranostics. Ivyspring International Publisher. 2021; 2892–916 [cited 2025 Jan 16]. Available from: https://doi.org/10.7150/thno.50928.

Han S, Bao X, Zou Y, Wang L, Li Y, Yang L, et al. d -lactate modulates M2 tumor-associated macrophages and remodels immunosuppressive tumor microenvironment for hepatocellular carcinoma [Internet]. Sci. Adv. American Association for the Advancement of Science (AAAS). 2023. [cited 2025 Jan 16]. Available from: https://doi.org/10.1126/sciadv.adg2697

Hao X, Zheng Z, Liu H, Zhang Y, Kang J, Kong X, et al. Inhibition of APOC1 promotes the transformation of M2 into M1 macrophages via the ferroptosis pathway and enhances anti-PD1 immunotherapy in hepatocellular carcinoma based on single-cell RNA sequencing [Internet]. Redox Biol. Elsevier BV. 2022; 102463 [cited 2025 Jan 16]. Available from: https://doi.org/10.1016/j.redox.2022.102463.

Hashemi Goradel N, Najafi M, Salehi E, Farhood B, Mortezaee K. Cyclooxygenase-2 in cancer: A review [Internet]. J Cell Physiol. Wiley. 2018; 5683–99 [cited 2025 Jan 16]. Available from: https://doi.org/10.1002/jcp.27411.

He L, Jhong J-H, Chen Q, Huang K-Y, Strittmatter K, Kreuzer J, et al. Global characterization of macrophage polarization mechanisms and identification of M2-type polarization inhibitors [Internet]. Cell Rep. 2021;37:109955. https://doi.org/10.1016/j.celrep.2021.109955. Elsevier BV; [cited 2025 Jan 16].

Hong R, Xu B. Breast cancer: an up-to-date review and future perspectives [Internet]. Cancer Commun. 2022;42:913–36. https://doi.org/10.1002/cac2.12358. Wiley; [cited 2025 Jan 16].

Huang S, Xu Z, Wang J, et al. Macrophage membrane-mediated targeted curcumin biomimetic nanoparticles delivery for diagnosis and treatment of spinal cord injury by suppressing neuroinflammation and ferroptosis. Chem Eng J. 2024;500:157285. https://doi.org/10.1016/j.cej.2024.157285. [Internet].

Huo W, Yang X, Wang B, Cao L, Fang Z, Li Z, et al. Biomineralized hydrogel DC vaccine for cancer immunotherapy: A boosting strategy via improving immunogenicity and reversing immune-inhibitory microenvironment [Internet]. Biomaterials. Elsevier BV. 2022; 121722 [cited 2025 Jan 16]. Available from: https://doi.org/10.1016/j.biomaterials.2022.121722.

Husain S, Nandi A, Simnani FZ, Saha U, Ghosh A, Sinha A, et al. Emerging Trends in Advanced Translational Applications of Silver Nanoparticles: A Progressing Dawn of Nanotechnology [Internet]. JFB. MDPI AG. 2023; 47 [cited 2025 Jan 16]. Available from: https://doi.org/10.3390/jfb14010047.

Ji P, Gong Y, Jin M, Wu H, Guo L-W, Pei Y-C, et al. In vivo multidimensional CRISPR screens identify Lgals2 as an immunotherapy target in triple-negative breast cancer [Internet]. Sci. Adv. American Association for the Advancement of Science (AAAS). 2022. [cited 2025 Jan 16]. Available from: https://doi.org/10.1126/sciadv.abl8247.

Jiang LQ, Wang TY, Webster TJ, Duan H-J, Qiu JY, Zhao ZM, et al. Intracellular disposition of chitosan nanoparticles in macrophages: intracellular uptake, exocytosis, and intercellular transport [Internet]. IJN. Informa UK Limited. 2017; 6383–98 [cited 2025 Jan 16]. Available from: https://doi.org/10.2147/ijn.s142060.

Jiang X-Q. Establishment and characterization of a cell line, EH-GB2, derived from hepatic metastasis of gallbladder cancer [Internet]. Oncol Rep. Spandidos Publications. 2011. [cited 2025 Jan 16]. Available from: https://doi.org/10.3892/or.2011.1570.

Karim AM, Eun Kwon J, Ali T, Jang J, Ullah I, Lee Y-G, et al. Triple-negative breast cancer: epidemiology, molecular mechanisms, and modern vaccine-based treatment strategies [Internet]. Biochem Pharmacol. Elsevier BV. 2023; 115545 [cited 2025 Jan 16]. p. 115545. Available from: https://doi.org/10.1016/j.bcp.2023.115545.

Kazimierczak P, Koziol M, Przekora A. The Chitosan/Agarose/NanoHA Bone Scaffold-Induced M2 Macrophage Polarization and Its Effect on Osteogenic Differentiation In Vitro [Internet]. IJMS. MDPI AG. 2021; 1109 [cited 2025 Jan 16]. Available from: https://doi.org/10.3390/ijms22031109.

Khan MdA, Zafaryab Md, Mehdi SH, Ahmad I, Rizvi MMA. Characterization and anti-proliferative activity of curcumin loaded chitosan nanoparticles in cervical cancer [Internet]. Int J Biol Macromol. Elsevier BV. 2016; 242–53 [cited 2025 Jan 16]. Available from: https://doi.org/10.1016/j.ijbiomac.2016.08.050.

Larasati YA, Yoneda-Kato N, Nakamae I, Yokoyama T, Meiyanto E, Kato J. Curcumin targets multiple enzymes involved in the ROS metabolic pathway to suppress tumor cell growth [Internet]. Sci Rep. Springer Science and Business Media LLC. 2018. [cited 2025 Jan 16]. Available from: https://doi.org/10.1038/s41598-018-20179-6.

Lee HJ, Myung JK, Kim HS, Lee DH, Go HS, Choi JH, et al. Expression of LGR5 in mammary myoepithelial cells and in triple-negative breast cancers [Internet]. Sci Rep. Springer Science and Business Media LLC. 2021. [cited 2025 Jan 16]. Available from: https://doi.org/10.1038/s41598-021-97351-y.

Lee K, Lin C-C, Servetto A, Bae J, Kandagatla V, Ye D, et al. Epigenetic repression of STING by MYC promotes immune evasion and resistance to immune checkpoint inhibitors in triple-negative breast cancer [Internet]. Cancer Immunol Res. American Association for Cancer Research (AACR). 2022; 829–43. [cited 2025 Jan 16]. Available from: https://doi.org/10.1158/2326-6066.cir-21-0826.

Li H, Yang P, Wang J, Zhang J, Ma Q, Jiang Y, et al. HLF regulates ferroptosis, development and chemoresistance of triple-negative breast cancer by activating tumor cell-macrophage crosstalk [Internet]. J Hematol Oncol. Springer Science and Business Media LLC. 2022a. [cited 2025 Jan 16]. Available from: https://doi.org/10.1186/s13045-021-01223-x.

Li M, He L, Zhu J, Zhang P, Liang S. Targeting tumor-associated macrophages for cancer treatment [Internet]. Cell Biosci. Springer Science and Business Media LLC. 2022b. [cited 2025 Jan 16]. Available from: https://doi.org/10.1186/s13578-022-00823-5.

Li X, Li J, Xu L, Wei W, Cheng A, Zhang L, et al. CDK16 promotes the progression and metastasis of triple-negative breast cancer by phosphorylating PRC1 [Internet]. J Exp Clin Cancer Res. Springer Science and Business Media LLC. 2022c. [cited 2025 Jan 16]. Available from: https://doi.org/10.1186/s13046-022-02362-w.

Li Y, Zhang H, Merkher Y, Chen L, Liu N, Leonov S, et al. Recent advances in therapeutic strategies for triple-negative breast cancer [Internet]. J Hematol Oncol. Springer Science and Business Media LLC; 2022d [cited 2025 Jan 16]. Available from: https://doi.org/10.1186/s13045-022-01341-0.

Li C, Xu Y, Zhang J, Zhang Y, He W, Ju J, et al. The effect of resveratrol, curcumin and quercetin combination on immuno-suppression of tumor microenvironment for breast tumor-bearing mice [Internet]. Sci Rep. Springer Science and Business Media LLC. 2023. [cited 2025 Jan 16]. Available from: https://doi.org/10.1038/s41598-023-39279-z.

Liu Y, Peng Y, Du W, Yu C, Peng Z, Qin L, et al. PD-L1-mediated immune evasion in triple-negative breast cancer is linked to the loss of ZNF652 [Internet]. Cell Reports. Elsevier BV. 2023; 113343 [cited 2025 Jan 16]. Available from: https://doi.org/10.1016/j.celrep.2023.113343.

Liu Y, Zhang D, Zhang Z, Liang X, Yang X, Ding N, et al. Multifunctional nanoparticles inhibit tumor and tumor-associated macrophages for triple-negative breast cancer therapy [Internet]. J Colloid Interface Sci. Elsevier BV. 2024; 598–610 [cited 2025 Jan 16]. Available from: https://doi.org/10.1016/j.jcis.2023.11.156.

Luo C, Wang P, He S, Zhu J, Shi Y, Wang J. Progress and prospect of immunotherapy for triple-negative breast cancer [Internet]. Front Oncol. Frontiers Media SA. 2022. [cited 2025 Jan 16]. Available from: https://doi.org/10.3389/fonc.2022.919072.

Mahoutforoush A, Solouk A, Hamishehkar H, Haghbin Nazarpak M, Abbaspour-Ravasjani S. Novel decorated nanostructured lipid carrier for simultaneous active targeting of three anti-cancer agents [Internet]. Life Sci. Elsevier BV. 2021; 119576. [cited 2025 Jan 16]. Available from: https://doi.org/10.1016/j.lfs.2021.119576.

Mahoutforoush A, Asadollahi L, Hamishehkar H, Abbaspour-Ravasjani S, Solouk A, Haghbin Nazarpak M. Targeted Delivery of Pennyroyal via Methotrexate Functionalized PEGylated Nanostructured Lipid Carriers into Breast Cancer Cells; A Multiple Pathways Apoptosis Activator [Internet]. Adv Pharm Bull. Maad Rayan Publishing Company. 2023; 747–60. [cited 2025 Jan 16]. Available from: https://doi.org/10.34172/apb.2023.077.

Mehta AK, Cheney EM, Hartl CA, Pantelidou C, Oliwa M, Castrillon JA, et al. Targeting immunosuppressive macrophages overcomes PARP inhibitor resistance in BRCA1-associated triple-negative breast cancer [Internet]. Nat Cancer. Springer Science and Business Media LLC. 2020; 66–82 [cited 2025 Jan 16]. Available from: https://doi.org/10.1038/s43018-020-00148-7.

Moradpoor H, Safaei M, Mozaffari HR, Sharifi R, Imani MM, Golshah A, et al. An overview of recent progress in dental applications of zinc oxide nanoparticles [Internet]. RSC Adv. Royal Society of Chemistry (RSC). 2021; 21189–206 [cited 2025 Jan 16]. Available from: https://doi.org/10.1039/d0ra10789a.

Mukherjee S, Baidoo JNE, Fried A, Banerjee P. Using curcumin to turn the innate immune system against cancer [Internet]. Biochem Pharmacol. Elsevier BV. 2020; 113824. [cited 2025 Jan 16]. Available from: https://doi.org/10.1016/j.bcp.2020.113824.

Ning S, Wang C, Zhao L, Yang J, Shi X, Zheng Y. Lecithin/chitosan nanoparticle drug carrier improves anti-tumor efficacy of Monascus pigment rubropunctatin [Internet]. International Journal of Biological Macromolecules. Elsevier BV. 2023; 125058. [cited 2025 Jan 16]. Available from: https://doi.org/10.1016/j.ijbiomac.2023.125058.

Pal B, Chen Y, Vaillant F, Capaldo BD, Joyce R, Song X, et al. A single-cell RNA expression atlas of normal, preneoplastic and tumorigenic states in the human breast [Internet]. EMBO J. Springer Science and Business Media LLC. 2021. [cited 2025 Jan 16]. Available from: https://doi.org/10.15252/embj.2020107333.

Pang L, Pei Y, Uzunalli G, Hyun H, Lyle LT, Yeo Y. Surface Modification of Polymeric Nanoparticles with M2pep Peptide for Drug Delivery to Tumor-Associated Macrophages [Internet]. Pharm Res. Springer Science and Business Media LLC. 2019. [cited 2025 Jan 16]. Available from: https://doi.org/10.1007/s11095-019-2596-5.

Pérez-Núñez I, Rozalén C, Palomeque JÁ, Sangrador I, Dalmau M, Comerma L, et al. LCOR mediates interferon-independent tumor immunogenicity and responsiveness to immune-checkpoint blockade in triple-negative breast cancer [Internet]. Nat Cancer. Springer Science and Business Media LLC; 2022 [cited 2025 Jan 16]. p. 355–70. Available from: https://doi.org/10.1038/s43018-022-00339-4.

Popovic LS, Matovina-Brko G, Popovic M, Punie K, Cvetanovic A, Lambertini M. Targeting triple-negative breast cancer: A clinical perspective [Internet]. Oncol Res. Tech Science Press. 2023; 221–38 [cited 2025 Jan 16]. Available from: https://doi.org/10.32604/or.2023.028525.

Pu Y, Ji Q. Tumor-Associated Macrophages Regulate PD-1/PD-L1 Immunosuppression [Internet]. Front. Immunol. Frontiers Media SA. 2022. [cited 2025 Jan 16]. Available from: https://doi.org/10.3389/fimmu.2022.874589.

Rafiee F, Rezaee M. Different strategies for the lipase immobilization on the chitosan based supports and their applications [Internet]. Int J Biol Macromol. Elsevier BV. 2021; 170–95. [cited 2025 Jan 16]. Available from: https://doi.org/10.1016/j.ijbiomac.2021.02.198.

Ren S, Chang J, Liu R, Jin G. The novel selective TLR7 agonist GY101 suppresses colon cancer growth by stimulating immune cells [Internet]. Eur J Pharmacol. Elsevier BV. 2024; 176383. [cited 2025 Jan 16]. Available from: https://doi.org/10.1016/j.ejphar.2024.176383.

Rosa AD. Docking-based analysis and modeling of the activity of bile acids and their synthetic analogues on large conductance Ca2+ activated K channels in smooth muscle cells [Internet]. European Review. 2021. Available from: http://www.europeanreview.org/article/27449

Schinocca C, Rizzo C, Fasano S, Grasso G, La Barbera L, Ciccia F, et al. Role of the IL-23/IL-17 Pathway in Rheumatic Diseases: An Overview [Internet]. Front. Immunol. Frontiers Media SA. 2021. [cited 2025 Jan 16]. Available from: https://doi.org/10.3389/fimmu.2021.637829.

Shi L, Zhu W, Huang Y, Zhuo L, Wang S, Chen S, et al. Cancer-associated fibroblast-derived exosomal microRNA-20a suppresses the PTEN/PI3K-AKT pathway to promote the progression and chemoresistance of non-small cell lung cancer [Internet]. Clinical & Translational Med. Wiley; 2022 [cited 2025 Jan 16]. Available from: https://doi.org/10.1002/ctm2.989.

Tang W, Sun G, Ji G-W, Feng T, Zhang Q, Cao H, et al. Single-cell RNA-sequencing atlas reveals an FABP1-dependent immunosuppressive environment in hepatocellular carcinoma [Internet]. J Immunother Cancer. BMJ. 2023; e007030 [cited 2025 Jan 16]. Available from: https://doi.org/10.1136/jitc-2023-007030.

Tkach M, Thalmensi J, Timperi E, Gueguen P, Névo N, Grisard E, et al. Extracellular vesicles from triple negative breast cancer promote pro-inflammatory macrophages associated with better clinical outcome [Internet]. Proc Natl Acad Sci U.S.A. Proceedings of the National Academy of Sciences. 2022. [cited 2025 Jan 16]. Available from: https://doi.org/10.1073/pnas.2107394119.

Vasconcelos DP, Costa M, Amaral IF, Barbosa MA, Águas AP, Barbosa JN. Modulation of the inflammatory response to chitosan through M2 macrophage polarization using pro-resolution mediators [Internet]. Biomaterials. Elsevier BV.

2015. [cited 2025 Jan 16]. Available from: https://doi.org/10.1016/j.biomaterials.2014.10.035.

Vranic S, Cyprian FS, Gatalica Z, Palazzo J. PD-L1 status in breast cancer: Current view and perspectives [Internet]. Semin Cancer Biol. Elsevier BV. 2021; 146–54 [cited 2025 Jan 16]. Available from: https://doi.org/10.1016/j.semcancer.2019.12.003.

Wang J, Liu LG, Jiao W-Q, Yang H, Liu J, Liu D. Phenylboronic acid-conjugated chitosan nanoparticles for high loading and efficient delivery of curcumin [Internet]. Carbohydrate Polymers. Elsevier BV. 2021a; 117497 [cited 2025 Jan 16]. Available from: https://doi.org/10.1016/j.carbpol.2020.117497.

Wang S, Ma L, Wang Z, He H, Chen H, Duan Z, et al. Lactate Dehydrogenase-A (LDH-A) Preserves Cancer Stemness and Recruitment of Tumor-Associated Macrophages to Promote Breast Cancer Progression [Internet]. Front Oncol. Frontiers Media SA. 2021b; [cited 2025 Jan 16]. Available from: https://doi.org/10.3389/fonc.2021.654452.

Wang X, Tokheim C, Gu SS, Wang B, Tang Q, Li Y, et al. In vivo CRISPR screens identify the E3 ligase Cop1 as a modulator of macrophage infiltration and cancer immunotherapy target [Internet]. Cell. Elsevier BV. 2021c; 5357–5374.e22 [cited 2025 Jan 16]. Available from: https://doi.org/10.1016/j.cell.2021.09.006.

Wang M, Pan W, Xu Y, Zhang J, Wan J, Jiang H. Microglia-mediated neuroinflammation: A potential target for the treatment of cardiovascular diseases [Internet]. JIR. Informa UK Limited. 2022a; 3083–94 [cited 2025 Jan 16]. Available from: https://doi.org/10.2147/jir.s350109.

Wang Y, Wang X, Li Y, Xue Z, Shao R, Li L, et al. Xuanfei Baidu Decoction reduces acute lung injury by regulating infiltration of neutrophils and macrophages via PD-1/IL17A pathway [Internet]. Pharmacological Research. Elsevier BV. 2022b; 106083 [cited 2025 Jan 16]. Available from: https://doi.org/10.1016/j.phrs.2022.106083.

Wang Y, Yuan Y, Wang W, He Y, Zhong H, Zhou X, et al. Mechanisms underlying the therapeutic effects of Qingfeiyin in treating acute lung injury based on GEO datasets, network pharmacology and molecular docking [Internet]. Computers in Biology and Medicine. Elsevier BV. 2022c; 105454 [cited 2025 Jan 16]. Available from: https://doi.org/10.1016/j.compbiomed.2022.105454.

Wang C, Xu Y-H, Xu H-Z, Li K, Zhang Q, Shi L, et al. PD-L1 blockade TAM-dependently potentiates mild photothermal therapy against triple-negative breast cancer [Internet]. J Nanobiotechnol. Springer Science and Business Media LLC. 2023a. [cited 2025 Jan 16]. Available from: https://doi.org/10.1186/s12951-023-02240-3.

Wang W, Li M, Wang L, Chen L, Goh B-C. Curcumin in cancer therapy: Exploring molecular mechanisms and overcoming clinical challenges [Internet]. Cancer Letters. Elsevier BV. 2023b; 216332 [cited 2025 Jan 16]. Available from: https://doi.org/10.1016/j.canlet.2023.216332.

Weng Y-S, Tseng H-Y, Chen Y-A, Shen P-C, Al Haq AT, Chen L-M, et al. MCT-1/miR-34a/IL-6/IL-6R signaling axis promotes EMT progression, cancer stemness and M2 macrophage polarization in triple-negative breast cancer [Internet]. Mol Cancer. Springer Science and Business Media LLC. 2019. [cited 2025 Jan 16]. Available from: https://doi.org/10.1186/s12943-019-0988-0.

Wu Y, Yi Z, Li J, Wei Y, Feng R, Liu J, et al. FGFR blockade boosts T cell infiltration into triple-negative breast cancer by regulating cancer-associated fibroblasts [Internet]. Theranostics. Ivyspring International Publisher. 2022; 4564–80 [cited 2025 Jan 16]. Available from: https://doi.org/10.7150/thno.68972.

Xu J, Qin S, Yi Y, Gao H, Liu X, Ma F, et al. Delving into the Heterogeneity of Different Breast Cancer Subtypes and the Prognostic Models Utilizing scRNA-Seq and Bulk RNA-Seq [Internet]. IJMS. MDPI AG. 2022; 9936 [cited 2025 Jan 16]. Available from: https://doi.org/10.3390/ijms23179936.

Yang F, Xiao Y, Ding J-H, Jin X, Ma D, Li D-Q, et al. Ferroptosis heterogeneity in triple-negative breast cancer reveals an innovative immunotherapy combination strategy [Internet]. Cell Metab. Elsevier BV. 2023; 84–100.e8 [cited 2025 Jan 16]. Available from: https://doi.org/10.1016/j.cmet.2022.09.021.

Yu CC, Wortman JC, He T-F, Solomon S, Zhang RZ, Rosario A, et al. Physics approaches to the spatial distribution of immune cells in tumors [Internet]. Rep Prog Phys. IOP Publishing. 2021; 022601 [cited 2025 Jan 16]. Available from: https://doi.org/10.1088/1361-6633/abcd7b.

Yu F, Luo H, Wang Y, Wei Z, Li B, Zhao Y, et al. Preparation of curcumin-loaded chitosan/lecithin nanoparticles with increased anti-oxidant activity and in vivo bioavailability [Internet]. Int J Biol Macromol. Elsevier BV. 2024; 136659. [cited 2025 Jan 16]. Available from: https://doi.org/10.1016/j.ijbiomac.2024.136659.

Zhang B, Shetti D, Fan C, Wei K. miR-29b-3p promotes progression of MDA-MB-231 triple-negative breast cancer cells through downregulating TRAF3 [Internet]. Biol Res. Springer Science and Business Media LLC. 2019. [cited 2025 Jan 16]. Available from: https://doi.org/10.1186/s40659-019-0245-4.

Zhang Y, Fan Y, Jing X, Zhao L, Liu T, Wang L, et al. OTUD5-mediated deubiquitination of YAP in macrophage promotes M2 phenotype polarization and favors triple-negative breast cancer progression [Internet]. Cancer Lett. Elsevier BV. 2021; 104–15. [cited 2025 Jan 16]. Available from: https://doi.org/10.1016/j.canlet.2021.02.003.

Zhang M, Zhang X, Tian T, Zhang Q, Wen Y, Zhu J, et al. Anti-inflammatory activity of curcumin-loaded tetrahedral framework nucleic acids on acute gouty arthritis [Internet]. Bioact Mater. Elsevier BV. 2022a; 368–80. [cited 2025 Jan 16]. Available from: https://doi.org/10.1016/j.bioactmat.2021.06.003.

Zhang R, Yang Y, Dong W, Lin M, He J, Zhang X, et al. D-mannose facilitates immunotherapy and radiotherapy of triple-negative breast cancer via degradation of PD-L1 [Internet]. Proc Natl Acad Sci U.S.A. Proceedings of the National Academy of Sciences. 2022b. [cited 2025 Jan 16]. Available from: https://doi.org/10.1073/pnas.2114851119.

Zhang H, Zhu S, Zhou H, Li R, Xia X, Xiong H. Identification of MTHFD2 as a prognostic biomarker and ferroptosis regulator in triple-negative breast cancer [Internet]. Front Oncol. Frontiers Media SA. 2023a. [cited 2025 Jan 16]. Available from: https://doi.org/10.3389/fonc.2023.1098357.

Zhang J, Lu S, Lu T, Han D, Zhang K, Gan L, et al. Single-cell analysis reveals the COL11A1+ fibroblasts are cancer-specific fibroblasts that promote tumor progression [Internet]. Front Pharmacol. Frontiers Media SA. 2023b. [cited 2025 Jan 16]. Available from: https://doi.org/10.3389/fphar.2023.1121586.

Zhang R, Shen Y, Zhang Q, Feng X, Liu X, Huo X, et al. TRIM21-mediated Sohlh2 ubiquitination suppresses M2 macrophage polarization and progression of triple-negative breast cancer [Internet]. Cell Death Dis. Springer Science and Business Media LLC. 2023c. [cited 2025 Jan 16]. Available from: https://doi.org/10.1038/s41419-023-06383-x.

Zhang X, Wei Z, Yong T, Li S, Bie N, Li J, et al. Cell microparticles loaded with tumor antigen and resiquimod reprogram tumor-associated macrophages and promote stem-like CD8+ T cells to boost anti-PD-1 therapy [Internet]. Nat Commun. Springer Science and Business Media LLC. 2023d. [cited 2025 Jan 16]. Available from: https://doi.org/10.1038/s41467-023-41438-9.

Zhao J, Zhang Y, Liu X, Zhu F, Xie F, Jiang C, et al. RNA-binding protein Musashi2 stabilizing androgen receptor drives prostate cancer progression [Internet]. Cancer Sci. Wiley. 2020; 369–82 [cited 2025 Jan 16]. Available from: https://doi.org/10.1111/cas.14280.

Zhou Z, Lin S, Yue T, et al. Adsorption of food dyes from aqueous solution by glutaraldehyde cross-linked magnetic chitosan nanoparticles. J Food Eng. 2014;126:133–41. https://doi.org/10.1016/j.jfoodeng.2013.11.014. [Internet].

Zhou C, Yi C, Yi Y, Qin W, Yan Y, Dong X, et al. LncRNA PVT1 promotes gemcitabine resistance of pancreatic cancer via activating Wnt/β-catenin and autophagy pathway through modulating the miR-619-5p/Pygo2 and miR-619-5p/ATG14 axes [Internet]. Mol Cancer. Springer Science and Business Media LLC. 2020. [cited 2025 Jan 16]. Available from: https://doi.org/10.1186/s12943-020-01237-y.